Composites: Part A 204 (2026) 109643

Contents lists available at ScienceDirect

Composites Part A

journal homepage: www.elsevier.com/locate/compositesa

Characterizing and modelling the time-dependent compaction response of an infiltrated binder-stabilized unidirectional non-crimp fabric

Renan Miranda Portela [a], Bastian Schäfer [b,1], Luise Kärger [b], Alfredo Rocha de Faria [c], John Montesano [a,*]

[a] Composites Research Group, Mechanical & Mechatronics Engineering, University of Waterloo, 200 University Ave. West, Waterloo, ON N2L 3G1, Canada
[b] Karlsruhe Institute of Technology (KIT), Institute of Vehicle System Technology (FAST), Karlsruhe, Germany
[c] Department of Mechanical Engineering, Instituto Tecnológico de Aeronáutica (ITA), Praça Marechal Eduardo Gomes, 50, São José dos Campos, SP 12228-900, Brazil

ARTICLE INFO

Keywords:
Binder stabilized unidirectional non-crimp fabric
Infiltrated compaction experiments
Binder pre-activation
Viscoelastic modelling

ABSTRACT

In wet compression molding (WCM), understanding the compaction behavior of infiltrated reinforcement fabrics is essential, as it impacts the microstructure and fiber volume fraction of the finished part. Incorporating binder-stabilized reinforcements may be necessary in WCM to improve material handling and enhance part quality. This research aims to characterize and model the time-dependent compaction behavior of an infiltrated, binder-stabilized carbon fiber unidirectional non-crimp fabric (UD-NCF) through multi-phase experiments, specifically focusing on effects of resin viscosity, stacking sequence, and binder pre-activation. Findings indicate that infiltrated fabric requires lower compaction forces compared to dry fabric, mainly due to the lubrication of tows and stitching, which reduces tow-stitch friction and provides less resistance to tow spreading. Furthermore, compaction forces increase with binder pre-activation across all conditions tested, while the degree of relaxation is reduced. Lastly, the stacking sequence has a minor influence on the compaction response owing to limitations in tow nesting imposed by supporting fibers. Maxwell and fractional Zener models are considered to capture the fabric time-dependent response, with the latter providing an improved fit to the experimental data. This is the first detailed investigation on compaction behavior of infiltrated, binder-stabilized UD-NCFs, offering new and important insights into their complex deformation response.

1. Introduction

1.1. Research motivation

Wet Compression Molding (WCM) is a manufacturing process that is especially advantageous for mass production with highly reactive resins, owing to low cycle times. Specialized equipment such as metering units for resin injection or large presses are not required, which simplifies the process and lowers overall manufacturing costs. Poppe et al. [1] describe the direct variant of the WCM process (Fig. 1a), which involves five main steps: fabric cutting and stacking, resin application, stack insertion into the pre-heated mold, forming and molding, and curing followed by demolding the final composite component. A key characteristic of the direct variant is a simultaneous fabric forming and resin infiltration step. Conversely, the WCM process also has an indirect variant (Fig. 1b) that separates the forming and resin infiltration steps, resulting in an additional preforming step before resin application.

Manufacturing WCM parts involves continuous reinforcements such as woven and unidirectional non-crimp fabrics (UD-NCF). Woven fabrics typically offer improved drapability when compared to UD-NCFs. However, UD-NCFs have gained attention in several industry sectors as a suitable alternative for various liquid composite molding processes, including WCM. UD-NCF composites offer greater tailorability of anisotropic properties when compared to woven fabric-based composites, resulting in a greater lightweight potential [2]. UD-NCFs comprise aligned fiber tows that are held together by stitching yarns that ensure the structural integrity of the reinforcement and stabilize the fabric [2–5]. Thus, UD-NCF composites exhibit improved in-plane mechanical properties owing to the absence of interlacing, unlike woven fabrics, which enhances in-plane mechanical properties [6].

* Corresponding author.
E-mail address: john.montesano@uwaterloo.ca (J. Montesano).
[1] Current affiliation: SIMUTENCE GmbH, 76131 Karlsruhe, Germany.

https://doi.org/10.1016/j.compositesa.2026.109643
Received 26 November 2025; Received in revised form 3 February 2026; Accepted 5 February 2026
Available online 12 February 2026

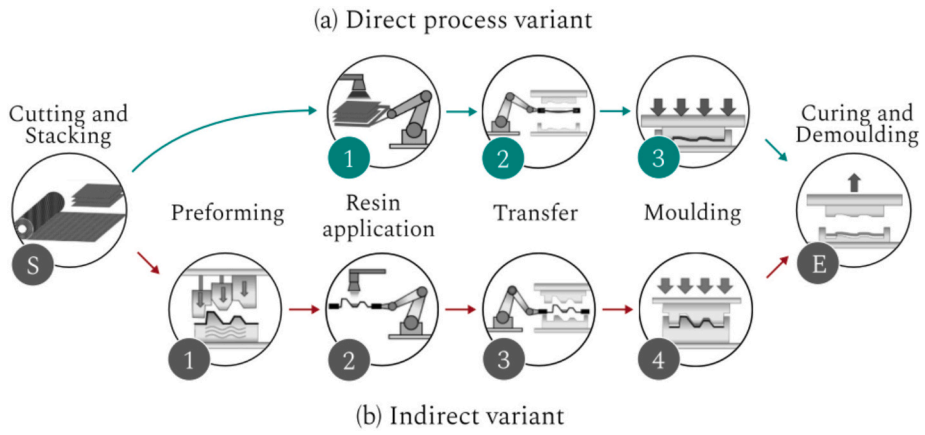

Fig. 1. Schematic of the wet compression molding (WCM) process steps: (a) direct variant, and (b) indirect variant [1].

When producing structural components that require multiple layers of UD-NCF with distinct orientations to meet specific performance requirements, the resulting WCM components can be relatively thick. Manufacturing such thick parts using the direct WCM process variant involves applying a substantial amount of resin onto the fabric stack and transferring into the mold. However, producing such components, especially in molds with deep cavities, presents challenges related to resin management as the UD-NCF stack may deform due to gravity prior to closure of the mold due to its limited bending stiffness. A promising solution to address this issue is the use of binder-stabilized UD-NCF, where pre-activation of the binder before application of the resin may provide increased fabric bending stiffness [7,8] and enable improved resin management. Stabilizing binders are either thermoplastic or uncatalyzed epoxy resins, available in either solvent-based liquid or dry powder form [9–11]. Stabilizing binders are typically used to keep fabric layers adhered to one another and maintain fabric integrity during operations such as trimming and handling [9], while they are necessary for preforming UD-NCF stacks. However, the use of binder-stabilized fabrics may also introduce challenges, as they can affect processing conditions and the formability of the fabric. Some of these challenges would also apply to the indirect WCM variant, where the binder-stabilized UD-NCF is preformed prior to introducing resin onto the fabric.

The study of fabric compaction is important due to its influence on the mold filling behavior and the tooling closing force, especially for the WCM process, and on the composition of the final composite part, including the fiber volume fraction and the resulting mechanical performance. Bickerton et al. [12] outline that during transverse compression, the stress–strain behavior of the fiber bed exhibits viscoelastic characteristics, which are influenced by the lubrication state. Yong et al. [13] state that for manufacturing processes with rigid-closed molds (i.e., WCM), the determination of whether the desired fiber volume fraction can be achieved is given by the reaction force on the tooling surface, which depends on the compaction response. Other characteristics of the fabric stack can also be affected by the compaction mechanism, such as the permeability of the fabric. Werlen et al. [14] explain that during compaction the fabric layers are forced to slide against each other and rearrange inside the mold, generating friction forces. In manufacturing processes like WCM the reinforcement fabric is typically lubricated during forming, where the friction between adjacent layers is reduced and the relative sliding between layers eases [13,14].

1.2. State-of-the-Art

1.2.1. Compaction behavior

Previous studies have examined the compaction behaviour of woven fabric stacks to identify the key influencing parameters. Poppe et al. [15] investigated the effects of shear angle, impregnation, and nesting on the compaction response of carbon fibre woven fabric stacks using a punch-to-plate setup. Experiments on unsheared and pre-sheared fabrics with shear angles of 25° and 50° showed that increasing shear angle leads to higher compaction stiffness and forces due to the increase in stack height and material density induced by shear deformation. The influence of pre-infiltration with silicone oil was also examined, revealing that the presence of an incompressible fluid generates additional pressure beneath the punch, thereby increasing the compressive force. Furthermore, fabric stacks with different stacking sequences (i.e., $[0]_4$ and $[0/45]_2$) were tested to assess yarn nesting. The experiments revealed that yarn nesting reduced stack stiffness and compressive force, with this effect being more pronounced when the fabric layers were aligned (i.e., $[0]_4$ stack). Additional studies have focused on the compaction mechanisms of non-crimp fabrics, considering various process parameters. Schäfer et al. [16] characterized UD- and biaxial-NCFs with different stacking sequences and fiber orientations at interfaces. It was noted that resistance to compaction decreases as the number of layers increases, although this effect diminishes beyond a certain number of layers. They also observed limited nesting in UD-NCFs compared to biaxial-NCFs, which can be attributed to the supporting fibers that are orthogonal to the carbon fiber tows, thereby preventing a more pronounced nesting effect in the UD-NCF layers. Li et al. [17] investigated the effects of cyclic compactions, number of layers, stitching patterns (such as tricot, chain, and tricot-chain), compression rate, and fabric impregnation for carbon fiber NCF. They found that lubrication has little impact on the compaction behavior due to low friction, but impregnation influences relaxation response. Nesting caused by impregnated stitching yarns was also noted by Droste et al. [18]. It is important to note that these studies did not consider the influence of stabilizing binder on the compaction response of UD-NCFs.

Additional research has examined the time-dependent compaction response of binder-stabilized fabrics. Wei et al. [19] analyzed the influence of different concentrations of liquid stabilizing binder (0%, 4%, 8%, and 12%) on the compression response of various carbon fiber textiles, including two types of woven fabrics, a biaxial NCF, and a multiaxial NCF. The authors observed that as the binder concentration increased, the elastic modulus decreased and the degree of stress relaxation was enhanced. In another study, Wei et al. [20] investigated the influence of process parameters (e.g., compression speed, maximum pressure, and holding time) on the compaction behavior of binder-stabilized fabric with different weight concentrations of binder. An increase in the initial stack thickness with increase in binder concentration was reported, while the recovery thickness increased with an increase of maximum pressure regardless of binder concentration. Additionally, they reported a possibility of raising the fiber volume fraction by reducing the compression rate. Although these studies reported important findings regarding the influence of the stabilizing binder on

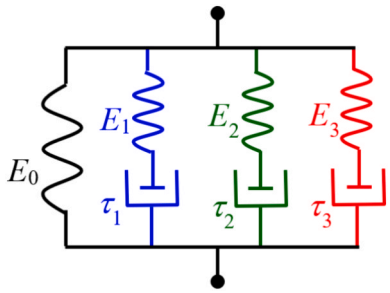

Fig. 2. Schematic of the three-branch Maxwell model, including an elastic and three viscoelastic branches. The illustrated elements are defined as: springs (Ei) and dashpot (τ_j) [14].

compaction behaviour of NCFs, they were limited to a liquid stabilizing binder and, thus, were unable to investigate the effect of binder pre-activation. Furthermore, these studies did not consider the influence of impregnation on the compaction behaviour of binder-stabilized fabric, which is critical for the WCM process. A comprehensive assessment of the inter-dependency between stabilizing binder and fabric impregnation and their role on the compaction behaviour of associated reinforcement fabrics is currently missing from the literature.

1.2.2. *Compaction modeling*

The compaction response of engineering textile stacks has been considered in several previous studies, with some of the early models being empirically based. Robitaille and Gauvin [21] compiled and analysed a broad range of experimental compaction and relaxation data for textile reinforcements and employed empirical constitutive relationships to characterise their behaviour. The compaction response was described using fitted parameters representing rigidity, initial fibre volume fraction, and a stiffening index, allowing general trends associated with the number of layers, material architecture, and loading history to be identified. These empirical models highlighted systematic shifts in compaction and relaxation behaviour with repeated loading, processing speed, and material type, and provided a basis for comparing different textile reinforcements. In contrast, Gutowski et al. [22] proposed a consolidation model that, while grounded in physical assumptions, relies on empirically validated relationships to describe the nonlinear elastic response of the fibre network and the strong dependence of permeability on fibre volume fraction and direction. Their model captured experimentally observed trends such as the resin pressure being lower than the applied pressure during consolidation, thereby linking empirical observations to process-relevant outcomes such as laminate thickness and local fibre volume fraction. Poppe et al. [15] developed and validated coupled finite element forming and fluid-submodels to simulate the three-dimensional WCM process. They stated that the forming submodel can reproduce the non-linear viscoelastic compaction response of a woven fabric stack without numerical locking. Mitsch et al. [23] proposed and validated a computationally efficient 3D modeling approach that includes nonlinear compaction modeling, enabling the simulation of the thermoforming process of thermoplastic composites. The nonlinear time-dependent nature of fabric compaction prompted the use of rheological-based material models, combining elastic springs and viscous dashpots, such as Maxwell, Burgers, and Zener models. In the Maxwell model, the viscoelastic behavior of a given material is described by a spring and dashpot in series. In the Burgers model, viscoelasticity is characterized by the combination of a spring and a dashpot in series (i.e., a Maxwell element) together with a spring and a dashpot in parallel (i.e., a Kelvin–Voigt element) [24,25]. Finally, the Zener model consists of a spring and a dashpot in series with a second spring in parallel [26]. Echaabi et. al. [27] compared all three rheological models and reported that the Maxwell model returned the most accurate results among the three for relaxation time. Danzi et al. [28] proposed a three-branch Maxwell model with strain-dependent springs and strain-rate-dependent dashpots (Fig. 2) to describe the time-dependent compaction response of a dry carbon fiber woven fabric bed. The authors reported that this model is valid across different fiber volume fractions and strain rates. The same three-branch Maxwell model was later adopted by Werlen et al. [14] for modelling the compaction response of fabric stacks comprising various types of fabrics. They reported that the three-branch Maxwell model yielded accurate results for a wide range of experimental configurations (e.g., fabric architecture, fiber volume fraction, and fabric impregnation state). However, modelling viscoelastic behavior is a challenging task and can require a considerable number of springs and dashpots to adequately fit to experimental data. The three-branch Maxwell model for a one-dimensional stress case requires calibration of seven parameters (E_0, E_1, τ_1, E_2, τ_2, E_3, τ_3) [29,30]. Da Costa-Haveroth et al. [30] state that these experiments can generate too many parameters to be identified and instead proposed the implementation of fractional derivatives. Fractional derivatives can adequately describe the viscoelastic behavior and provide effective curve-fitting with a lower mean square error and fewer input parameters [31,32]. Hence, the fractional Zener model was proposed as an alternative to the Maxwell model, replacing the viscoelastic branches (Fig. 2) by a spring-pot or Scott-Blair element, illustrated in Fig. 3a. The result of this replacement is a system with four parameters (E_0, E_1, α, p) as shown in Fig. 3b.

To obtain the material parameters that can accurately represent the time-dependent behavior of fabrics captured during experiments, an optimization method can be used. Several optimization methods have been adopted for this purpose, including Simplex and Particle Swarm Optimization (PSO). Werlen et al. [14] obtained the material parameters for the Maxwell model by applying a finite difference method, which was optimized with the Simplex optimization algorithm. This optimization approach was implemented, obtaining three parameters while the other four were fixed, which can lead to a time-consuming and

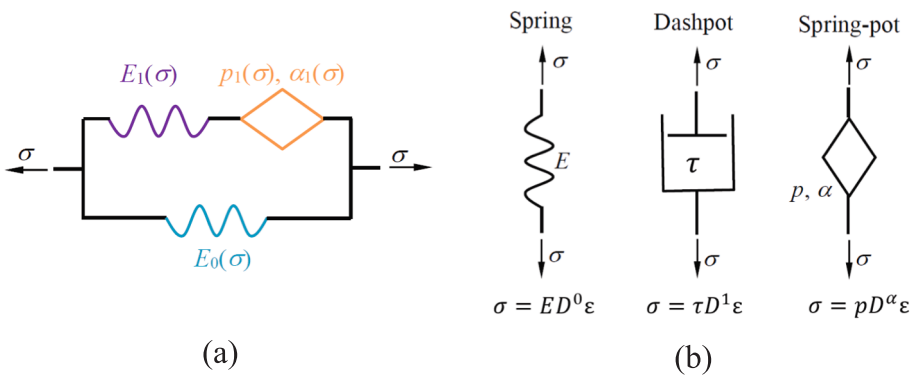

Fig. 3. Schematics of: (a) Fractional Zener model, and (b) rheological elements. The illustrated elements are defined as: springs (E_i), dashpots (τ_j), stress (σ), strain (ε), fractional derivative order (α), proportionality factor (p,) and the fractional derivative operator (D) [30].

computationally expensive optimization process. PSO is a heuristic method for inverse optimization problems in which the material parameters are sought to fit experimental curves [29,33]. The optimization process is heuristic due to a few or a lack of initial assumptions related to the optimized problem [30,34]. Although the PSO can provide no guarantee of global minimum value, the optimization process is capable of searching large domains of possible solutions and requires no use of gradients. For this reason, the optimization problem has no requirement of differentiability, and the PSO is extensively applied in optimization problems that present irregularities or numerical noises [29]. A potential alternative to the PSO method would be the well-known Gradient-based methods (e.g., gradient descent, conjugate gradient, Newton's method, sequential quadratic programming). However, those methods require differentiable objective functions and are more prone to local minima depending on the starting search point.

1.3. Research goal

While few studies have investigated the compaction behaviour of infiltrated non-crimp fabrics, these studies did not consider the influence of stabilizing binder. Moreover, limited studies have considered the influence of liquid stabilizing binder content on the compaction behaviour of non-crimp fabrics. However, these studies did not consider infiltrated fabrics nor the impact of pre-activating the binder and the inter-dependency with fabric impregnation on the compaction response. The review of the literature reveals a critical gap in compaction characterization of infiltrated, powder binder-stabilized UD-NCFs, which is critical for WCM processes. In recent work by the authors [8], the bending characteristics of a binder stabilized UD-NCF were assessed. It was found that infiltration of the fabric reduced bending stiffness when compared to the dry fabric, while pre-activation of the binder and increasing the loading rate notably increased bending stiffness. Nevertheless, the effect of binder pre-activation and infiltration fluid viscosity on the compaction behaviour of the fabric, which is a distinct deformation mechanism, cannot be deduced from the bending response. Therefore, the goal of the investigation herein is to characterize and model the time-dependent compaction response of an infiltrated, binder-stabilized UD-NCF stack, focusing on the effects of viscosity, binder pre-activation, and stacking sequence. A set of experiments was conducted whereby 8-layer bindered fabric stacks were subjected to compaction load relaxation cycles for eight distinct conditions. Both Maxwell and fractional Zener rheological models are fit to the compaction response data using the PSO method to establish the fabric stack compaction behavior parameters.

2. Methodology

2.1. Materials and specimen preparation

A binder-stabilized UD-NCF, specifically PX35-UD300 (Zoltek, US), was examined. The fabric comprises aligned 50 K continuous PX35 carbon fiber (CF) tows that are secured with a 76 dtex polyester yarn in a tricot pattern and supported with low linear density transversely oriented glass fiber (GF) yarns to enhance handleability. The textile also contains a thermosetting polymer powder binder dispersed on the side with the stitch tricot pattern, resulting in a total areal density of 333 g/m^2 (see Ref. [2] for further details). Square specimens measuring 100 mm × 100 mm were cut from a roll using an automated cutting table (Zünd Systemtechnik AG, Switzerland) in both 0° and 45° orientations. These layers were stacked with either a $[0]_8$ or $[0/45]_4$ sequence to mimic compaction of an 8-layer stack during the WCM process. A subset of the stacks was placed on trays in an industrial oven at 120°C for 20 min to pre-activate the stabilizing binder present on each layer of the stack. Additionally, some specimens were impregnated with silicone oils with either 20 cSt or 100 cSt viscosities—similar to that of various resins at elevated temperatures. The impregnation involved soaking the stack in a silicone oil bath for 15 min, then draining excess oil for another 15 min, as shown in Fig. 4.

2.2. Punch-to-plate compaction test

The compaction tests were performed using an Inspekt universal testing machine equipped with a 5 kN load cell and a 56 mm diameter metal punch and flat plate to compress the fabric sample (Fig. 5). It should be noted that the smaller footprint of the punch end surface ensured full contact with the fabric stack. This configuration allowed the force applied by the universal testing machine to be uniformly distributed over the corresponding region of the fabric specimen, thereby aiding to mitigate potential noise in the force measurements. However, the smaller footprint of the punch end may induce shear stresses in the specimen outside of the compacted region, which could influence the accuracy of the force measurement to some degree. The load cell measured the force, which was later converted into stress by dividing the force by the punch area, and the displacement was converted into strain by calculating the change in height divided by the initial stack height. It was ensured that the punch and flat plate were parallel by compressing the punch directly onto the plate surface and verifying uniform contact

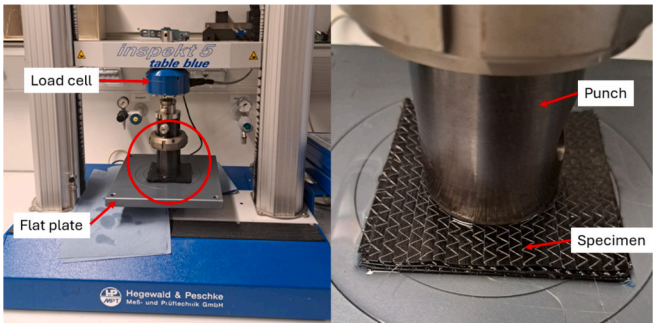

Fig. 5. Punch-to-plate compaction test setup for the 8-layer carbon fiber UD-NCF.

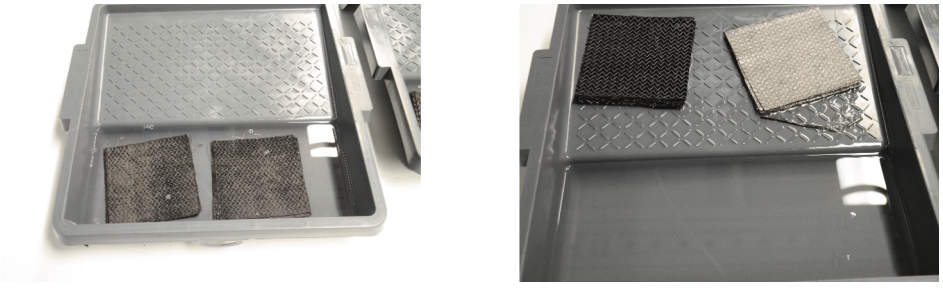

Fig. 4. Specimens soaking procedure: (a) silicone bath for 15 min to fully impregnate the stack, (b) drain process to remove the silicone excess.

between these surfaces before compacting the specimens. The stress–-strain values were used to obtain the compaction parameters. All compaction tests were conducted at room temperature under eight different conditions, four per stacking sequence (Table 1). For each stacking sequence, one condition involved dry samples without pre-activation of the stabilizing binder (IT), while for the other three conditions, the binder was pre-activated (AT). For two of these conditions, the samples were impregnated in silicone oil with a viscosity of 20 or 100 cSt. For each condition, four repeat tests were performed, yielding a total of 32 tests.

The loading cycle applied to the fabric stacks was similar to that used by Droste et al. [18] and comprised six phases (Fig. 6). The fabric response was captured during an initial compaction-relaxation cycle (i.e., Phases I − II) and the subsequent elastic recovery, while a second compaction-relaxation cycle (i.e., Phases V − VI) provided an assessment of the recompacted fabric response. The overall loading cycle mimics the preforming and infiltration steps in the WCM process variant shown in Fig. 1 (i.e., first and second compaction cycles), while the direct variant is represented by the first compaction cycle. Each test was performed in displacement control with a rate of 1 mm/min. During Phase I (i.e., first compaction), the punch was initially positioned 6 mm above the flat plate without contacting the stack specimen and displaced downwards to a pre-determined height of 2.5 mm to compact the sample. The onset of Phase I was identified at a predetermined time corresponding to the moment of contact between the punch and the stack, at which point the compaction force begins to increase. Phase II (i.e., first relaxation) commences at a predetermined time once the maximum compressive stress is attained and involves maintaining the stack at a constant height of 2.5 mm for a duration of 2 min. Phase III (i.e., first recovery) begins at a predetermined time with the reduction of force, allowing for a partial recovery of the stack's initial height. Phase IV commences once the force reaches a magnitude that is virtually 0 N, which is sustained for 5 min. Phase V begins thereafter where the stack is compressed for a second time to a height of 2.5 mm. Finally, Phase VI involves holding the pre-assigned height constant for 3 min.

Table 1
Conditions of the samples tested using the punch-to-plate compaction test setup, including different infiltrated fluid viscosities (dry, 20 cSt, and 100 cSt) and binder state (IT and AT).

Condition	Stacking sequence	Viscosity	Binder state	Number of tested specimens
1	$[0/45]_4$	Dry	IT	4
2	$[0/45]_4$	Dry	AT	4
3	$[0/45]_4$	20 cSt	AT	4
4	$[0/45]_4$	100 cSt	AT	4
5	$[0]_8$	Dry	IT	4
6	$[0]_8$	Dry	AT	4
7	$[0]_8$	20 cSt	AT	4
8	$[0]_8$	100 cSt	AT	4

The eight conditions were compared using different characterization metrics to better understand the influence of each parameter (e.g., pre-activation of the stabilizing binder and fabric impregnation). The first metric is the maximum compressive stress, which is defined by the maximum compressive load divided by the punch area. Another metric used in this study was the normalized relaxation stress λ, which is determined by:

$$\lambda = \frac{\sigma(t)}{\sigma_0}, \tag{1}$$

where $\sigma(t)$ is the variation of the stress during the relaxation phase, and σ_0 is the maximum compression stress at the end of the compression phase. A third metric used was the stress relaxation ratio (r), which characterizes the degree of stress relaxation and is defined by:

$$r = \frac{\sigma_0 - \sigma_f}{\sigma_0}, \tag{2}$$

where σ_f is the minimum compression stress at the end of the relaxation phase. Lastly, the elastic recovery ratio (e) represents the percentage of elastic compression deformation to the total deformation and is defined as:

$$e = \frac{h_e - h_f}{h_i - h_f} \tag{3}$$

where h_i is the height where the punch touches the stack, h_e is the height where the punch returns at the end of the recovery phase, and h_f is the height where the punch is set to compress the stack ($h_e = 2.50$mm).

To verify the statistical significance of the impregnation fluid viscosity, binder pre-activation, and stacking sequence on the compaction response, pairwise analyses were conducted on compaction response metrics for two conditions using a two-sample T-test. The null hypothesis for a T-test assumes no difference between the sample data and is accepted when the corresponding p-value is greater than 0.05. Otherwise, the null hypothesis is rejected, indicating a statistically significant difference.

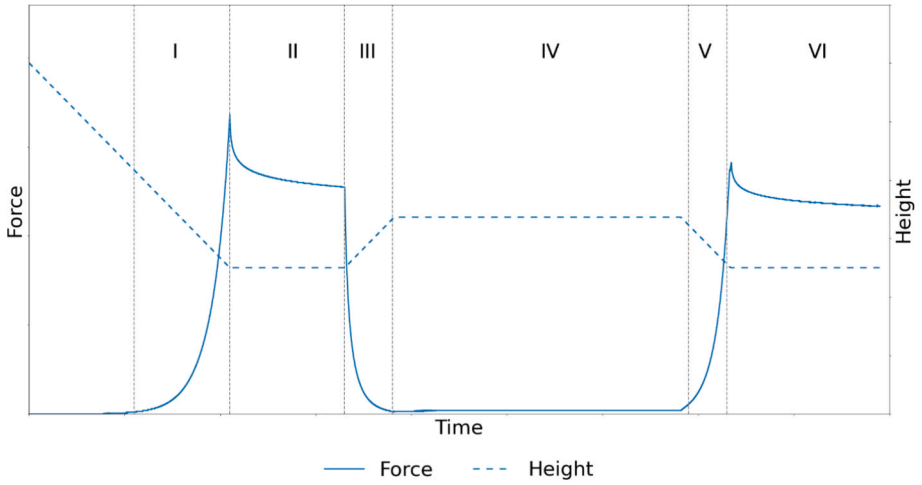

Fig. 6. Force-time and punch height-time profiles representing the two-cycle compaction-relaxation experiments performed on UD-NCF specimens. Phases I and II respectively correspond to the first compaction and stress relaxation cycle, Phase III corresponds to the initial recovery upon removal of force, Phase IV represents a zero-force dwell phase between cycles, while Phases V and VI respectively correspond to the second compaction and stress relaxation cycle.

2.3. Implementation of rheological models

Fitting of experimental data was divided into two parts: the compaction and relaxation phases. The compaction phase was modelled with a nonlinear three-branch Maxwell model implemented by Bublitz et al. [35] for the case of uniaxial stress. The first step involves calculating the elastic strain of each branch of the Maxwell model $\left(\varepsilon_j^e\right)$:

$$\varepsilon_j^{e,n+1} = \varepsilon_j^{e,n}\exp\left(-\frac{\Delta t}{\tau_j}\right) + \frac{\Delta\varepsilon}{\frac{\Delta t}{\tau_j}}\left(1-\exp\left(-\frac{\Delta t}{\tau_j}\right)\right), \tag{4}$$

where τ_j denotes the damper parameters and Δt the time step size. The elastic modulus of each viscoelastic branch is defined as:

$$E_j = a_j\exp\left((\varepsilon-\varepsilon^e)b_j\right), \tag{5}$$

where a_j and b_j are constant to be found, and ε is the total strain. Next, the stress in each viscoelastic branch is found by:

$$\sigma_j^{n+1} = \sigma_j^n\exp\left(-\frac{\Delta t}{\tau_j}\right) + \frac{\Delta\epsilon}{\frac{\Delta t}{\tau_j}}\left(E_j^{n+1} - E_j^n\left(-\frac{\Delta t}{\tau_j}\right)\right). \tag{6}$$

The j stress values are summed to the stress in the elastic branch, which varies with the fiber volume fraction (V_f). The V_f is defined as:

$$V_f = \frac{NA_w}{\rho_{fiber}h}, \tag{7}$$

where N denotes the number of layers, A_w represents the areal weight, ρ_{fiber} is the fabric density, and h the stack thickness. In this model, the fiber volume fraction influences the elastic modulus of the elastic branch, which is defined as:

$$E_0 = \frac{A}{V_f}\exp\left(BV_f^2\right), \tag{8}$$

where A and B are constant parameters to be determined. Finally, stresses are defined as:

$$\sigma^{n+1} = E_0\varepsilon^{n+1} + \sum_{j=1}^{N}\sigma_j^{n+1}, \tag{9}$$

The time-dependent compaction behavior or relaxation was captured using both the Maxwell and fractional Zener one-dimensional viscoelastic models. The Maxwell model, shown in Fig. 2, involves seven parameters $(E_0, E_1, \tau_1, E_2, \tau_2, E_3, \tau_3)$. Conversely, the fractional Zener model replaces the three spring and damper branches with a spring-pot element (see Fig. 3a), reducing the number of parameters to four (E_0, E_1, p, α), as illustrated in Fig. 3b. To capture the viscoelastic behavior using the Maxwell model, the time-dependent one-dimensional stress is defined as [28,33,36,37]:

$$\sigma(t) = \sigma_0 + \sum_{j=1}^{n}\sigma_j(t), \tag{10}$$

where σ_0 represents the elastic stress, $\sigma_j(t)$ are the time-dependent stress terms, and n is the number of viscoelastic branches. Eq. (10) can be rewritten to represent the viscoelastic stress in terms of the spring constants (k_j), damper parameters, and the fabric strain, given by:

$$\sigma(t) = \left\{k_0 + \sum_{j=1}^{n}k_j\exp\left(-\frac{t}{\tau_j}\right)\right\}\varepsilon(t). \tag{11}$$

Haveroth [29,30] presented in detail the fractional Zener method as an alternative to capture nonlinear viscoelasticity, where the one-dimensional constitutive equation is given by:

$$\sigma(t) + \frac{p}{E_1}D_t^\alpha\sigma(t) = E_0\varepsilon(t) + p\frac{E_0+E_1}{E_1}D_t^\alpha\varepsilon(t), \tag{12}$$

where α, E_0, E_1, and p are material parameters that must be determined. E_0 and E_1 represent the sprigs of the elastic and viscoelastic portion of the Fractional Zener model, respectively (see Fig. 3). Schmidt and Gaul [38] highlight that the value of α varies from 0 to 1. When $\alpha = 0$, the spring-pot element behaves as a spring, and the parameter p represents the spring stiffness. On the other hand, when $\alpha = 1$, the spring-pot element assumes a damper behavior, and the material parameter p represents the damper viscosity. D_t^α is the fractional derivative defined by Grünwald-Letnikov (GL) as:

$$D_t^\alpha f(t) = (\Delta t)^{-\alpha}\sum_{m=0}^{N-1}A_{m+1}f_m, \tag{13}$$

where $f(t)$ is a regular function with $f_m = f(t-mt/N)$, $\Delta t = t/N(N>0)$ is the time increment, and A_{m+1} are the GL coefficients defined as:

$$A_{m+1} = \frac{\Gamma(m-\alpha)}{\Gamma(-\alpha)\Gamma(m+1)} = \frac{m-1-\alpha}{m}A_m, \tag{14}$$

where Γ represents the usual Gamma function and $A_0 = 1$. Substituting Eq. (13) into Eq. (12):

$$\sigma(t) + \frac{p}{E_1}\Delta t^{-\alpha}\sum_{m=0}^{N-1}A_{m+1}\sigma_m = E_0\varepsilon(t) + p\left(\frac{E_0+E_1}{E_1}\right)\Delta t^{-\alpha}\sum_{m=0}^{N-1}A_{m+1}\varepsilon_m, \tag{15}$$

with $\sigma_m := \sigma(t-m\Delta t)$ and $\varepsilon_m := \varepsilon(t-m\Delta t)$. Separating the first term of the sum on both sides:

$$\sum_{m=0}^{N-1}A_{m+1}\beta_m = \beta_0 + \sum_{m=1}^{N-1}A_{m+1}\beta_m, \tag{16}$$

where β denotes either σ or ε. With such a relation, Eq. (15) can be rewritten as:

$$\begin{aligned}\sigma(t)\left(1+\frac{p}{E_1}\Delta t^{-\alpha}\right) + \frac{p}{E_1}\Delta t^{-\alpha}\sum_{m=1}^{N-1}A_{m+1}\sigma_m \\ = \varepsilon(t)\left(E_0 + p\left(\frac{E_0+E_1}{E_1}\right)\Delta t^{-\alpha}\right) + p\left(\frac{E_0+E_1}{E_1}\right)\Delta t^{-\alpha}\sum_{m=1}^{N-1}A_{m+1}\varepsilon_m,\end{aligned} \tag{17}$$

and simplified to:

$$\sigma(t)(1+a) + aS_\sigma = \varepsilon(t)(E_0+b) + bS_\varepsilon, \tag{18}$$

where

$$a = \frac{p}{E_1}\Delta t^{-\alpha}, \tag{19}$$

$$b = p\left(\frac{E_0+E_1}{E_1}\right)\Delta t^{-\alpha}, \tag{20}$$

$$S_\sigma = \sum_{m=1}^{N-1}A_{m+1}\sigma_m, \tag{21}$$

$$S_\varepsilon = \sum_{m=1}^{N-1}A_{m+1}\varepsilon_m. \tag{22}$$

By solving Eq. (18) for $\sigma(t)$, the following is obtained:

$$\sigma(t) = \varepsilon(t)\frac{E_0+b}{1+a} + \frac{b}{1+a}S_\varepsilon - \frac{a}{1+a}S_\sigma. \tag{23}$$

The Maxwell and fractional Zener models were fitted to the compaction test data, and their respective parameters were determined using an optimization procedure. To save computational time, the material parameters were optimized using a vector of twenty-two experimental force values, spaced five seconds apart. These values were taken from Phase II of the compaction tests (Fig. 6), and stresses were

computed. The inverse optimization problem was defined as:

$$\text{Minimize} f : \mathbb{R}^n \rightarrow \mathbb{R} \tag{24}$$

where f is the objective function given by:

$$\ell^2\text{norm: } f(X) = \sqrt{\sum_{n=1}^{N} \left(\sigma_{\text{exp}}^{(n)} - \sigma_{\text{num}}^{(n)}(X)\right)^2}, \tag{25}$$

with $\sigma_{\text{exp}}^{(n)}$ and $\sigma_{\text{num}}^{(n)}$ being the experimental and numerical stresses, respectively. N represents the number of points, and $\overline{X}$ is the design variable vector. For the Maxwell model, the design vector is given by $\overline{X} = \{E_0, E_1, \tau_1, E_2, \tau_2, E_3, \tau_3\}^T$, also known as Prony-7. This design vector can be reduced to four variables (Prony-4) by setting the $\tau_i, i = 1, 2, 3$ to constant values, as suggested in Ref. [39]. However, the Maxwell model may present greater error, as shown in Ref. [30]. For the fraction Zener model, the design vector is given by $\overline{X} = \{\alpha, p, E_0, E_1\}^T$. To obtain the material parameters, both rheological models were optimized by using the PSO method, where the Python library pymoo [40] was used. The optimization process was performed with a population size of 7,000 points distributed in the search region by the latin hypercube sampling method [41]. The optimization was performed with a maximum of 60,000 evaluations and 100 generations, which required an average of 120 s CPU time per condition for the Maxwell model and an average of 90 s CPU time per condition for the Zenner model on a PC with an 8th Generation Intel Core i7-8700 Processor (3.20 GHz, 6 cores) and 16 GB DDR4 RAM.

3. Results and discussion

3.1. Experimentally captured compaction response

To ensure data consistency across all conditions (Table 1), force and height values were interpolated within the relevant time range for the four specimens tested. For each condition, the mean and standard deviation of force were computed from the sample sets, represented as solid lines and shaded regions in Fig. 7. The results across all tested conditions showed high repeatability with minimal variation in all phases. During the first compaction cycle (i.e., Phase I), all the samples exhibited a similar nonlinear deformation response with the forces nearly overlapping prior to reaching the peak force. Variation in the maximum compressive force was observed for the samples corresponding to the different conditions tested. The relaxation response during Phase II was also pronounced for each condition considered. During subsequent unloading (i.e., Phase III), both force and height measurements exhibited minimum variation. On the other hand, during the first dwell (i.e., Phase IV), samples for each condition exhibited a slightly different elastic recovery capacity. Additionally, it was observed that the specimens were not homogeneous in terms of the duration of their elastic recovery, which was evident through the shift in the height measurements with time among the different conditions. This variation with respect to time was more evident during the second compaction cycle (i.e., Phase V). Moreover, in the second compaction cycle, the measurements of maximum force exhibited notable variation among the different conditions, as in the first compaction cycle. For each condition, the magnitude of the peak force was lower during the second compaction cycle when compared to the first cycle. This result is in part due to the limited tow nesting ($[0]_8$ specimens, see Fig. 7c) and/or crimping ($[0/45]_4$ specimens) exhibited during the first compaction cycle, which required a greater magnitude of force. During the second compaction cycle, less force was required to achieve the same punch height. Lastly, the extent of stress relaxation during the second relaxation cycle (i.e., Phase VI) was notably less pronounced when compared to the first relaxation cycle for all conditions. Given that the specimens were already compacted during the initial cycle, increased resistance to specimen deformation and, thus, a lower degree of relaxation was

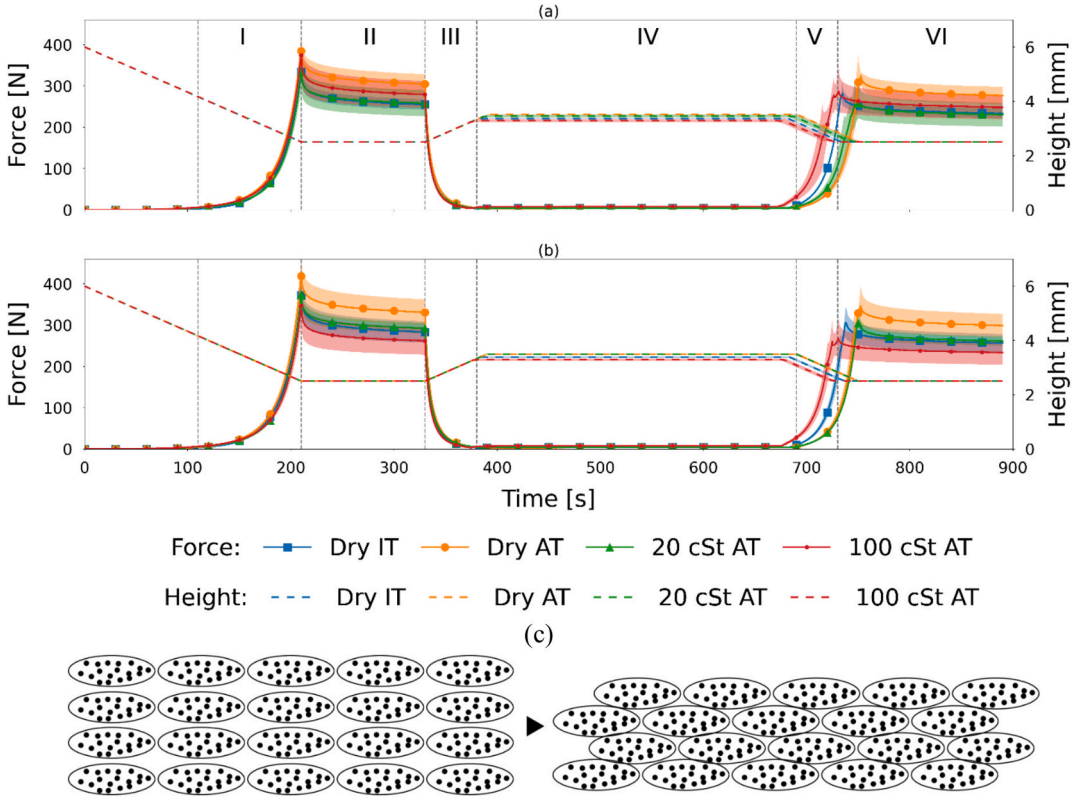

Fig. 7. Compaction force response and punch height-time data for: (a) $[0]_8$ stacking sequence (Conditions (5)–(8), and (b) $[0/45]_4$ stacking sequence (Conditions (1)–(4). The Conditions cover different infiltration fluid viscosities as well as inactive (IT) and pre-activated (AT) binder states, see Table 1. (c) Schematic of the tow nesting phenomenon for $[0]_8$ specimens during Phase I.

exhibited during this phase. The subsequent sections provide an in-depth quantitative analysis of the results for each loading phase, with emphasis on the influence of binder pre-activation, stacking sequence, and infiltrated fluid viscosity on the compaction response of the samples.

3.1.1. *Influence of the stabilizing binder pre-activation*

During the first and fifth stages of loading, i.e., the initial and second compaction cycles, the Dry AT specimens exhibited greater average maximum compression stress in comparison to the Dry IT specimens for both stacking sequences considered (Fig. 8). Fig. 9 depicts the maximum compression stress (σ_0) for each of the eight conditions for the first (Fig. 9(a) and 9(b)) and second (Fig. 9(c) and 9(d)) compaction cycles. A difference in the average maximum stress between the Dry AT and Dry IT specimens of 15% and 13% was observed for the first compression cycle, and 15% and 14% for the second compression cycle for $[0]_8$ and $[0/45]_4$ specimens, respectively. Increased peak stress for the Dry AT specimens is due to the increased resistance to tow deformation caused by the activated binder that has coated the tows. However, these differences were not statistically significant, as shown in Table A.1.1. The average maximum compression stresses for the second compaction cycle were less than that of the first compaction cycle for each of the Dry IT and Dry AT specimens owing to limited tow nesting/crimping, although the difference was not statistically significant (Table A.1.2). The similarity between the maximum stress measurements in different compression cycles has been reported by Li et al. [17] for a carbon fiber non-crimp fabric. Some permanent deformation during the first two cycles was reported; however, the maximum stress remained within a similar range, which could be attributed to the capacity of the stack to recover. Grieser and Mitschang [42] have also reported a reduction in compaction stress as a result of repetitive compaction cycles.

Next, a comparison is conducted between the relaxation responses during Phases II and VI (Fig. 7(a)), where the relaxation stress was normalized per Eq. (1). Fig. 10 illustrates the normalized relaxation stress for each relaxation cycle for both stacking sequences. It is

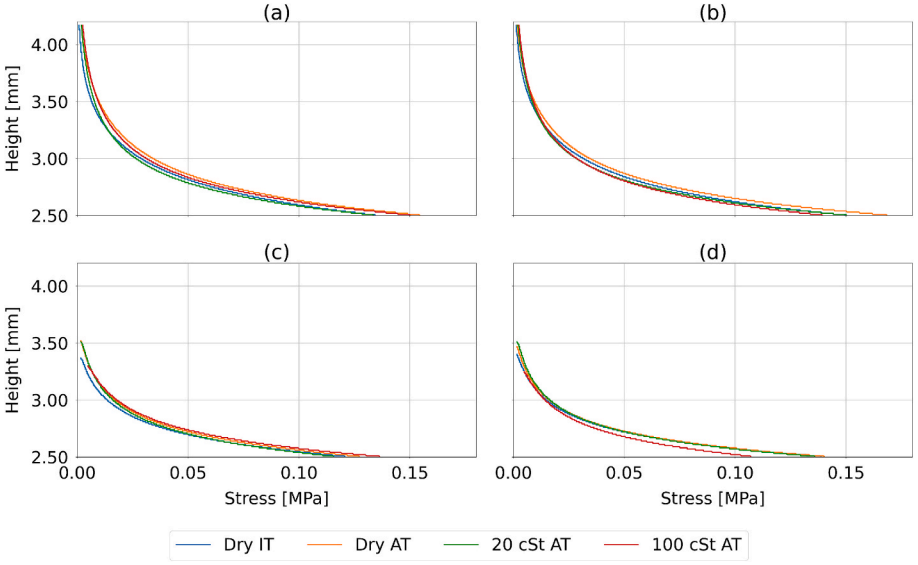

Fig. 8. Compression height-stress curves for the first compression cycle: (a) $[0]_8$, and (b) $[0/45]_4$ specimens, and the second compression cycle: (c) $[0]_8$, and (d) $[0/45]_4$ specimens.

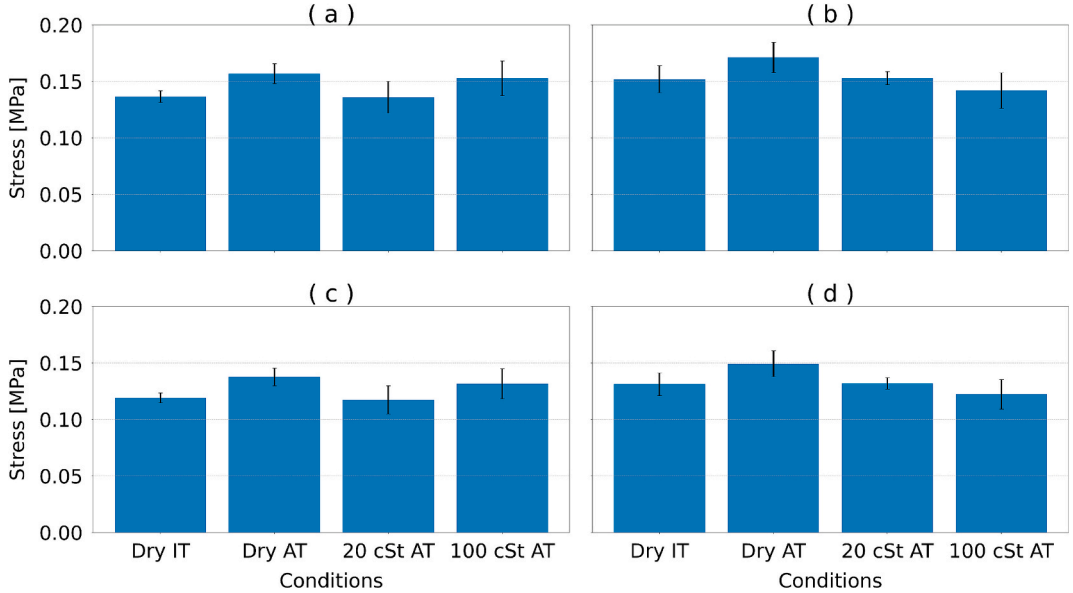

Fig. 9. Maximum compression stress (σ_0) for each impregnated condition: (a) first compaction cycle for $[0]_8$ specimen, (b) first compaction cycle for $[0/45]_4$ specimen, (c) second compaction cycle for $[0]_8$ specimen, and (d) second compaction cycle for $[0/45]_4$ specimen.

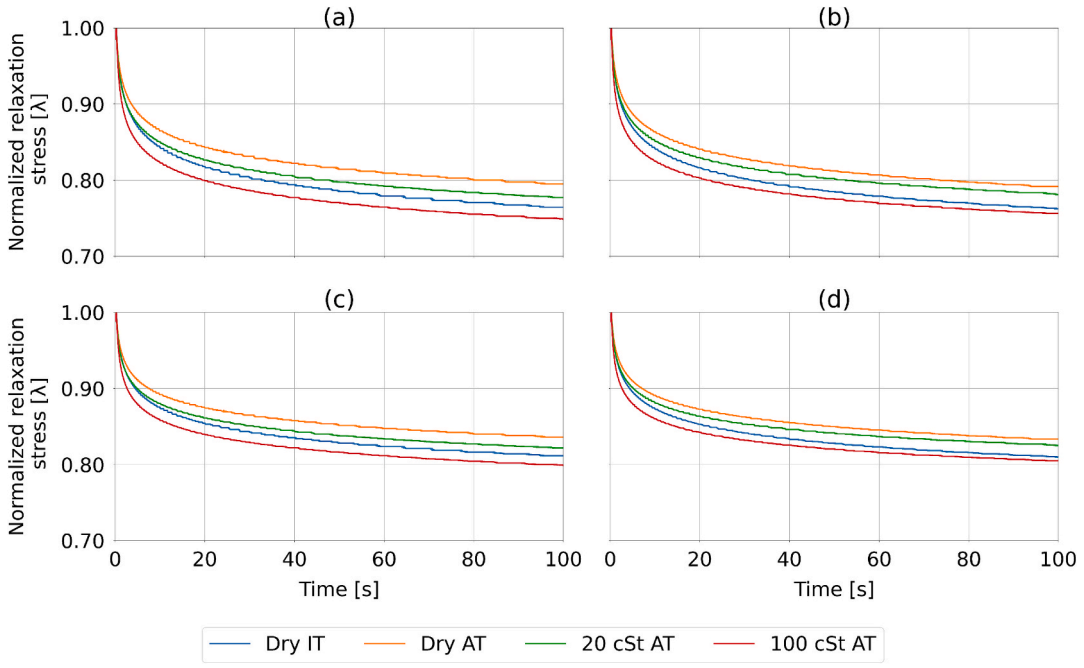

Fig. 10. Normalized relaxation stress for each impregnated condition: (a) first relaxation cycle for $[0]_8$ specimen, (b) first relaxation cycle for $[0/45]_4$ specimen, (c) second relaxation cycle for $[0]_8$ specimen, and (d) second relaxation cycle for $[0/45]_4$ specimen.

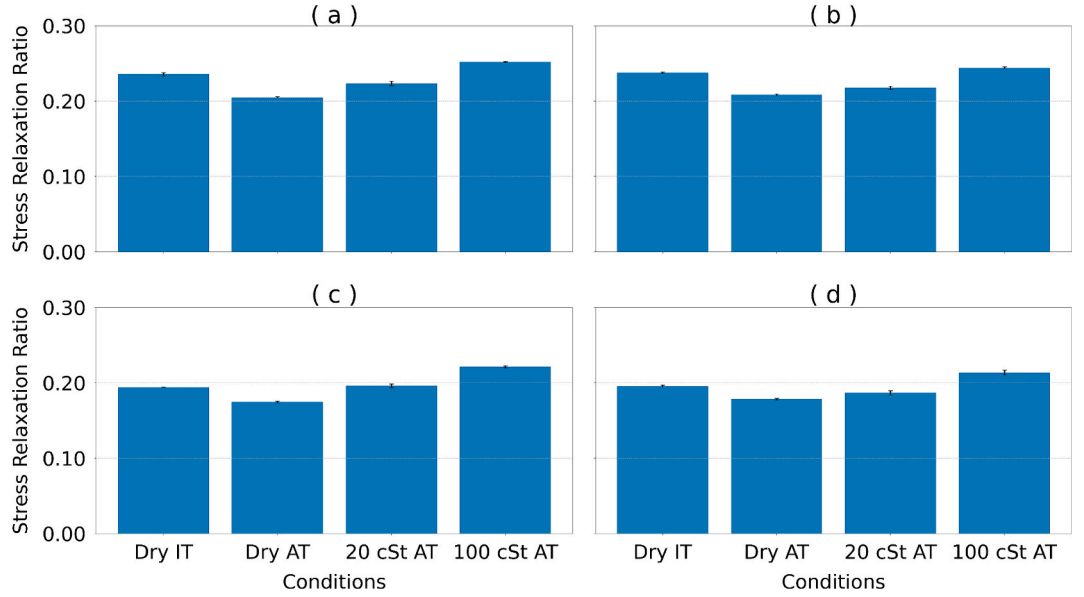

Fig. 11. Stress relaxation ratio for each impregnated condition: (a) first relaxation cycle for $[0]_8$, (b) first relaxation cycle for $[0/45]_4$, (c) second relaxation cycle for $[0]_8$, and (d) second relaxation cycle for $[0/45]_4$.

observed that for all four cases, the degree of relaxation for the Dry IT specimens was greater than that of the Dry AT specimens. A difference in the stress relaxation ratio of 15% and 14% was observed between the Dry IT and Dry AT specimens during the first relaxation cycle and 12% and 10% during the second relaxation cycle for the stacking sequences $[0]_8$ and $[0/45]_4$, respectively (Fig. 11). Activation of the stabilizing binder resulted in a statistically significant difference in the degree of relaxation (Table A.1.3). The reduced degree of relaxation observed for the Dry AT specimens can be attributed to the increased cohesion between the fiber tows resulting from the melting of the stabilizing binder. Conversely, for the Dry IT specimens, the layers were allowed to more readily shift relative to one another, thereby enabling greater relaxation.

It is also observed that the degree of stress relaxation during the first relaxation cycle for the Dry IT and Dry AT specimens (Fig. 10 (a) and (b)) is greater than that during the second relaxation cycle (Fig. 10 (c) and (d)), which was shown to be statistically significant (Table A.1.4). Similar outcomes were reported by Li et al. [17], where minor relaxation during the eighth cycle was attributed to a process that weakens the fabric stiffness after several cycles.

The elastic recovery of the Dry IT and Dry AT specimens after the recovery phase (i.e., Phase IV) was also compared (Fig. 12). Dry IT specimens for both stacking sequences exhibited a greater elastic recovery than the Dry AT specimens, specifically 20% greater for the $[0]_8$ stack and 4% greater for the $[0/45]_4$ stacking sequence. The reduced

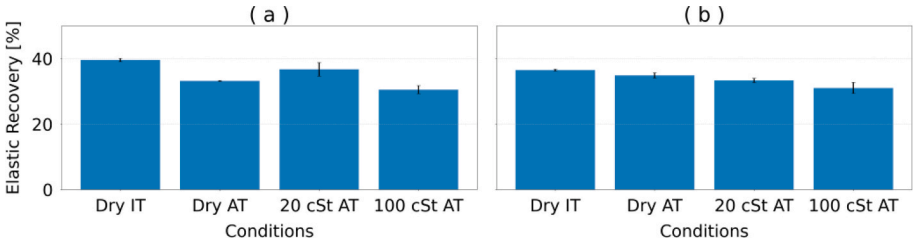

Fig. 12. Elastic recovery capacity for each impregnated condition during Phase IV: (a) $[0]_8$ and (b) $[0/45]_4$.

elastic recovery for the Dry AT specimens is due to increased resistance to deformation owing to cohesion between the layers caused by the activated binder. Statistical analysis points out that the elastic recovery of the Dry AT specimens is significantly different from that of the Dry IT specimens (Table A.1.5). Note, although the height of the punch was greater for the Dry AT specimens during the dwell phase when compared to the Dry IT specimens (Fig. 7(a)), the initial contact height of the punch was also higher for the former specimens. This finding is analogous with the results reported in Ref. [20], which emphasized that the addition of a stabilizing binder increases the initial stack thickness.

In the current study, the fabric stack was compressed to 2.5 mm, which is equivalent to a fiber volume fraction of 55% based on a calculation using the fabric areal weight. Schäfer et al. [16] investigated the same type of fabric without a stabilizing binder, which allows a better understanding of the influence of the thermosetting powder on the compaction response of the fabric. They indicate that the compression of a $[0]_8$ stacking sequence by up to 55% should result in a maximum stress of approximately 0.08 MPa. This stress magnitude is approximately 60% of the maximum compression stress for the Dry IT specimens with the same stacking sequence and half of the stress of the Dry AT specimens. This difference in maximum stress revealed the influence of the thermosetting powder binder on the compaction behavior of the studied fabric and is due to greater resistance to deformation for binder-stabilized fabrics. These findings align with the results in Ref. [20], which states that maximum compression stress increases with increasing binder content for the same thickness.

3.1.2. *Influence of the stacking sequence*

The influence of stacking sequence on the overall compaction response is demonstrated through the force response and punch height-time results in Fig. 7 (a) and (b). By comparing the maximum compression stress for the first compaction cycle (Fig. 9 (a) and (b)) and second compaction cycle (Fig. 9 (c) and (d)) for all conditions considered, the influence of stacking sequence is deemed to be minor. Table A.1.6 presents the p-values derived from the T-Test comparing the maximum compression stress values for both stacking sequences, with no statistical significance identified in any comparison.

The degree of relaxation for specimens with each stacking sequence was found to be similar for each condition, for both loading cycles (compare Fig. 11(a) and 11(b), and Fig. 11(c) and 11(d)). However, for the configurations in which the fabric stack was infiltrated with a 100 cSt oil, a statistical difference (see Table A.1.7) between the degree of relaxation for specimens with different stacking sequences was observed. Given that the difference was observed in specimens impregnated with 100 cSt oil in both cycles, exhibiting greater relaxation for the $[0]_8$ specimens, it can be inferred that this phenomenon may be attributable to the higher viscosity of the oil.

The final comparison between specimens with different stacking sequences focuses on the difference in elastic recovery during Phase IV (Fig. 12). Specimens with a $[0]_8$ stacking sequence exhibited an 8% increase in elastic recovery compared to specimens with a $[0/45]_4$ stacking sequence for the Dry IT condition. This phenomenon observed for the $[0]_8$ specimens can be attributed to enhanced recovery caused by the supporting glass fiber and stitching yarns that tended to aid with denesting of fiber tows. Statistical analysis (Table A.1.8) indicates that the stacking sequence has no influence on the recovery of the stack thickness for the remaining conditions.

The three analyses indicate a minor influence of the stacking sequence on compaction responses (i.e., maximum compression stress, degree of relaxation, and elastic recovery). This outcome aligns with the results documented in Refs. [16] and [43] that studied the compaction response of UD-NCF stacks. Both studies indicate that the low influence of the stacking sequence on the compaction response is due to the stitching yarns, especially when arranged in a tricot pattern. Lomov et al. [43] explain that the nesting process in non-crimp fabric is associated with the presence of gaps between tows; however, tricot stitching yarns limit a pronounced nesting effect when all the layers are aligned (i.e., $[0]_n$), leaving gaps between the layers.

3.1.3. *Influence of the infiltrated fluid viscosity*

The effect of fluid viscosity was also analyzed by comparing the maximum compression stress, relaxation response, and elastic recovery for the associated stages of loading. Generally, the maximum compression stress for the infiltrated specimens (20 and 100 cSt) was less than that of the Dry AT specimens and comparable to the Dry IT specimens for both compaction cycles and stacking sequences (Fig. 9). The peak compaction force for the Dry AT specimens exceeded those of the 20 cSt and 100 cSt specimens by 15.45% and 2.72% for the $[0]_8$ stack, and by 11.95% and 20.65% for the $[0/45]_4$ stack. The p-values presented in the last three columns of Table A.1.1 demonstrate that specimen impregnation does not result in a statistically significant influence on the maximum compression stress values. This result aligns with the findings documented in Ref. [17], which investigated the compaction of a 16-layer carbon fiber UD-NCF stack. It was concluded that lubrication does not significantly influence the peak compaction stress, which is attributed to the inherently low coefficient of friction of carbon fiber. Given that the carbon fiber already possesses a low friction coefficient, the impregnation of the fabric did not reduce friction substantially further, this only slightly affecting the peak stress values.

Fig. 10 (a) and (b) illustrate a comparison between dry samples and specimens impregnated with 20 cSt and 100 cSt silicone oil during the initial relaxation phase for each stacking sequence. The Dry AT specimens exhibited less relaxation compared to the infiltrated specimens for all stacking sequences and both compaction cycles, with the specimens infiltrated with 100 cSt oil exhibiting the greatest relaxation for every case (Fig. 11). Also, the degree of relaxation for the Dry IT specimens was comparable to that of the infiltrated specimens for all cases. This is explained by the increase in the friction coefficient in the Dry AT, which prevents the movement of adjacent layers and results in lower stress relaxation. On the other hand, the fabric impregnation reduces the friction coefficient caused by the melting of the stabilizing binder, easing the relaxation. These variations in relaxation are corroborated by the statistical analysis. Table A.1.3 presents the p-values obtained through the T-test, indicating a statistically significant difference among the conditions.

Finally, the influence of fluid viscosity on elastic recovery was examined, where Dry AT and infiltrated specimens exhibited similar elastic recovery (Fig. 12), with statistically minor differences for most

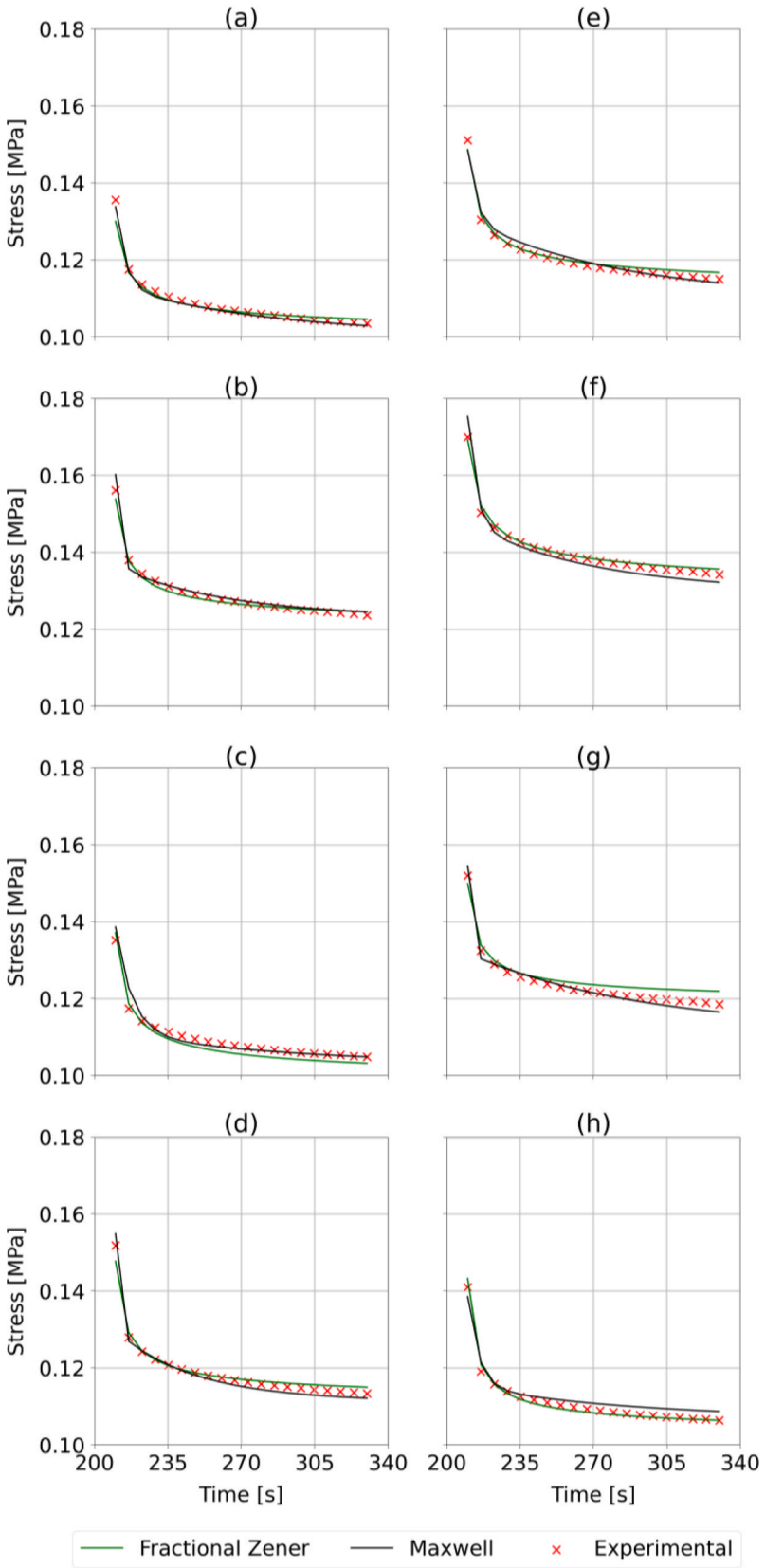

Fig. 13. Phase II stress-time curve fitting by using Fractional Zener and Maxwell models: (a) dry inactivated $[0]_8$, (b) dry pre-activated $[0]_8$, (c) impregnated 20 cSt pre-activated $[0]_8$, (d) impregnated 100 cSt pre-activated $[0]_8$, (e) dry inactivated $[0/45]_4$,(f) dry pre-activated $[0/45]_4$, (g) impregnated 20 cSt pre-activated $[0/45]_4$, and (h) impregnated 100 cSt pre-activated $[0/45]_4$.

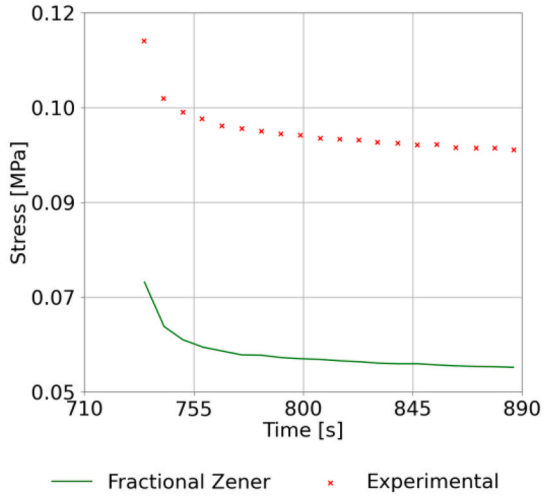

Fig. 14. A comparison between the experimental measurements of condition (4) during Phase VI and the curve derived from the material parameters obtained in Phase II using the Fractional Zener model.

cases (Table A.1.5).

3.2. Model parameter identification

As mentioned in Section 2.3, the stress values extracted from the average curve of the first compaction (Phase I) and relaxation (Phase II) cycle were used to obtain the material parameters and fit the time-dependent curve using the Fractional Zener and Maxwell models (Fig. 13). First, the relaxation phase was modelled. Table A.2.1 shows the parameters for the fractional Zener model obtained under each condition investigated during the first relaxation phase, and Table A.2.2 lists the material parameters for the Maxwell model for each condition during the first relaxation phase. For the first relaxation phase, both models fitted the experimental curves well with R^2 greater than 0.92 (Table A.2.1 and A.2.2). Both Table A.2.1 and A.2.2 reveal variations in the material parameter values from one condition to another. Wei et al. [19] suggested that the relaxation time (τ) increases with the concentration of liquid stabilizing-binder in weight. However, it was observed in these experiments and the curve-fitting process that the pre-activation of the stabilizing binder in powder form causes a reduction in the relaxation time.

As the fractional Zener has fewer variables, it is easier to attribute physical meaning to the values and compare the influence of each condition. Conditions (1) and (5) represent the inactivated stabilizing binder conditions for the stacking sequences $[0/45]_4$ and $[0]_8$, respectively, while conditions (2) and (6) represent the conditions with the binder activated thermally. Comparing the main elastic modulus (E_0) for both stacking sequences, an increase of 18% is observed from condition (1) to (2) and 20% from condition (5) to (6). Additionally, the elastic modulus of the spring in the viscoelastic branch (E_1) increased by 213% and 48% from the Dry IT to the Dry AT specimens for the $[0/45]_4$ and $[0]_8$, respectively. Those increases in the elastic moduli represent a greater resistance of the binder-activated stack in comparison to the inactivated stack. This is due to the molten binder [44], which, as it melts, coats the fiber tows and enhances the cohesion between the adjacent layers. This enhanced cohesion prevents the layers from shifting relative to one another, resulting in greater resistance to the compression applied by the punch. A comparison of the derivative order values (α) revealed reductions of 3.34% and 5.30% from the Dry IT to the Dry AT specimens for the $[0/45]_4$ and $[0]_8$, respectively. This implies that by activating the stabilizing binder, the stack assumes a behavior more akin to that of a spring, whereas the Dry IT specimens exhibit behavior more akin to a dashpot, which is characterized by greater stress relaxation.

Although the parameters listed in Tables A.1.1 and A.1.2 fit the curves Phase II of the experiment for each condition, they do not accurately reproduce the curve seen in Phase VI, as shown in Fig. 14 for the Fractional Zener for Condition (4). This deviation can be attributed to the limited nesting of the fabrics after the first compression-relaxation cycle, which affects the compaction behavior during the second cycle (Section 3.1), as well as the permanent deformation of the stack that causes the relaxation curves to flatten [17]. Reproducing the procedure conducted to obtain the material parameters in Phase II, the curve in Phase VI was fitted with each model, as illustrated in Fig. 15 (a) and (b). The parameters obtained for each condition are listed in Tables A.2.3 and A.2.4. This difference in arrangement exhibited a greater elastic modulus during the second relaxation, $E_0^{6th} > E_0^{2nd}$, which explains the greater compaction stress when comparing the experimental values in Phase VI and the stress estimation using values extracted from Phase II (Fig. 14). For Phase VI, both rheological models adequately fit the curves, albeit with a lower efficiency compared to the first relaxation cycle ($R^2 > 0.8$). However, the Maxwell model poorly captured some of the studied conditions (Fig. 15 (g) and (h)), in which $R^2$was less than0.8.

While both rheological models can generally be well fit to the experimental data, the Maxwell model is computationally more expensive due to the number of variables to be extracted, resulting in longer optimization processes. Additionally, the Fractional Zener has proven to be more efficient compared to the three-branch Maxwell model, with higher coefficients of determination (R^2).

Lastly, a generalized Maxwell model with nonlinear terms, which was developed by Kaliske and Rothert [45] and adapted by Bublitz et al. [35], was utilized to fit the compaction response of the fabric specimens during Phase I. Fig. 16 illustrates the stress-height curve during the first compaction cycle (i.e., Phase I) with the nonlinear Maxwell model fit for the eight configurations. Table A.2.5 lists the 11 material parameters obtained for each stacking sequence. In general, the model was well fitted with 7,000 experimental data points and 60,000 evaluations over the compaction phase. However, in some cases (refer to Fig. 16b, 16e, and 16f), the model did not achieve good agreement with the experimental data for lower heights, slightly overshooting the stress values. The greater difference between the experimental and numerical values in those three cases can be attributed to the significant number of parameters to be optimized and the large search area for each parameter.

4. Conclusions

The influence of binder pre-activation, stacking sequence, and impregnation fluid viscosity on the compaction response of an eight-layer carbon fiber unidirectional non-crimp fabric (UD-NCF) stack was investigated. Pre-activating the stabilizing binder increased the peak compaction stress by >10% when compared to a non-activated bindered fabric stack, owing to the increased resistance to tow deformation and enhanced cohesion among fabric layers, which restricted relative deformation. Additionally, pre-activating the stabilizing binder reduced the degree of relaxation of the stack by up to 15% and the recovery of the stack by up to 20%. Moreover, the stacking sequence was found to have minimal influence on the compaction response for the conditions considered, which is aligned with previous studies. The stitching yarns and supporting glass fibers limited pronounced tow nesting, for both stacking sequences considered, which ultimately limited inter-layer interactions and led to similar peak compressive forces and relaxation response for a given condition. Moreover, the fabric impregnation had no significant impact on the peak compaction stress due to the inherently low friction of the carbon fibers, rendering any reduction in friction between the fibers and stitching caused by the fluid to be minimal. On the other hand, the degree of relaxation was influenced by the infiltration of the fabric stack, which reduced tow friction and resistance

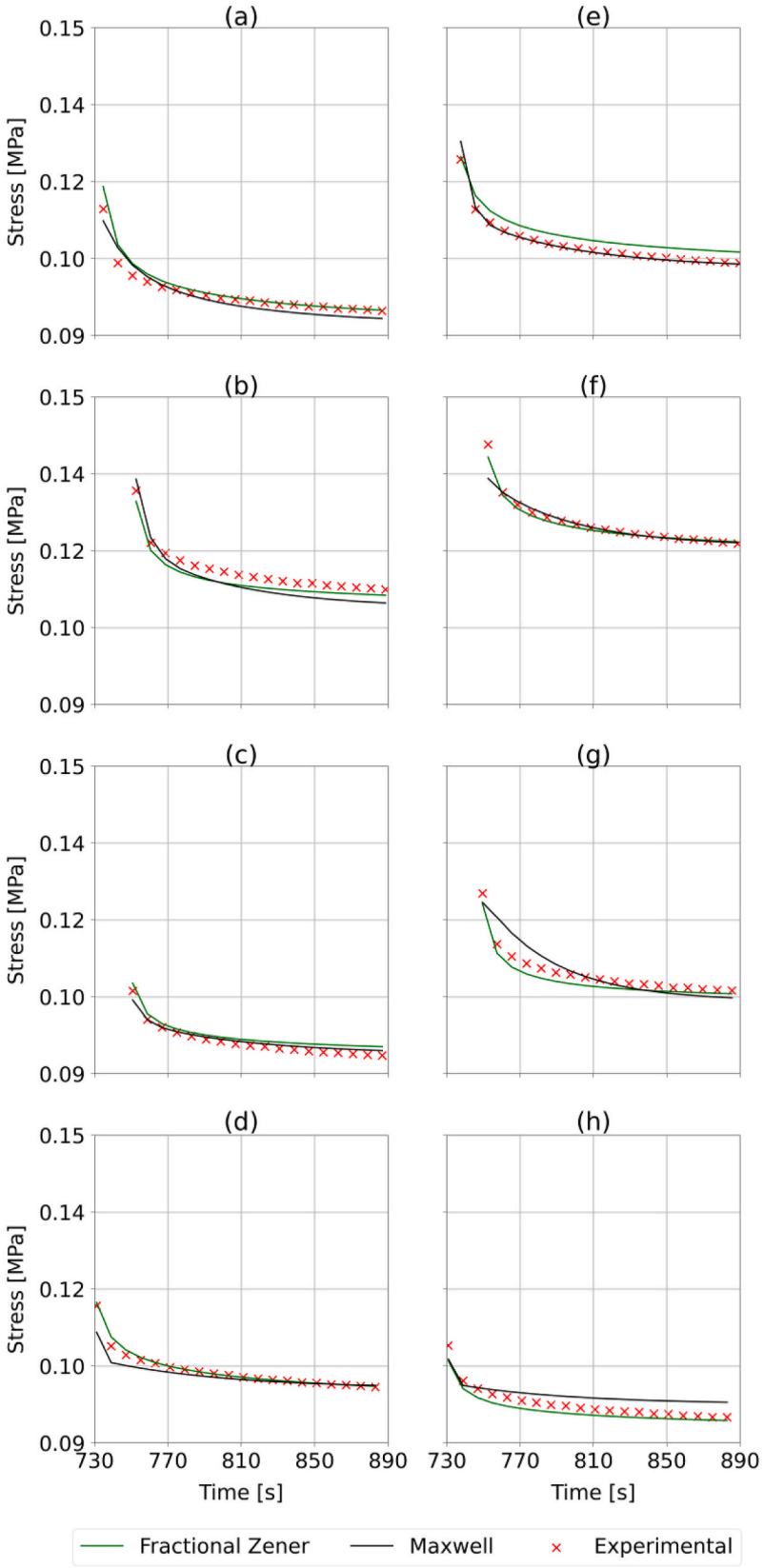

Fig. 15. Phase VI stress-time curve fitting by using Fractional Zener and Maxwell models: (a) dry inactivated $[0]_8$, (b) dry pre-activated $[0]_8$, (c) impregnated 20 cSt pre-activated $[0]_8$, (d) impregnated 100 cSt pre-activated $[0]_8$, (e) dry inactivated $[0/45]_4$,(f) dry pre-activated $[0/45]_4$, (g) impregnated 20 cSt pre-activated $[0/45]_4$, and (h) impregnated 100 cSt pre-activated $[0/45]_4$.

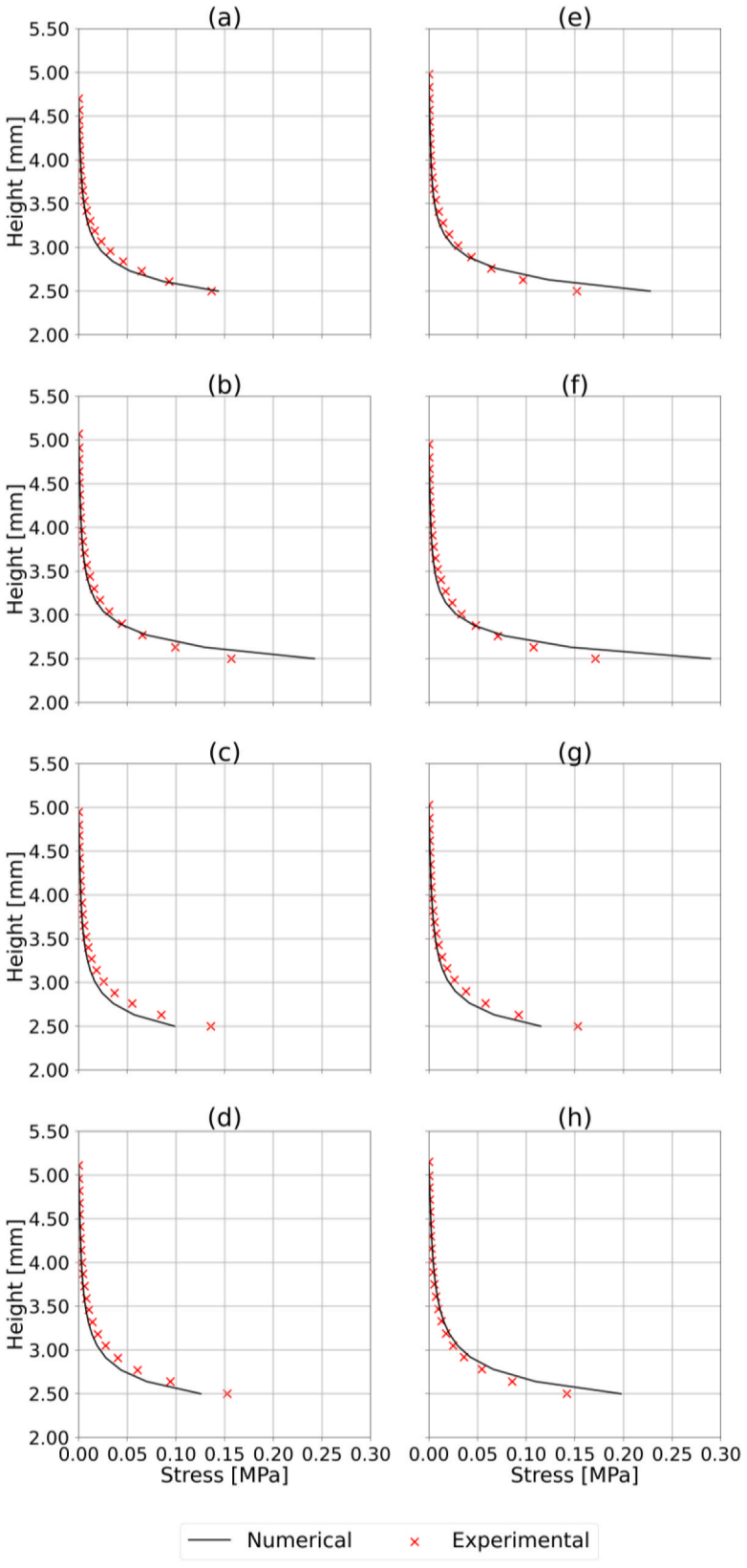

Fig. 16. Phase I height-stress curve fitting by using the nonlinear Maxwell model for: (a) dry inactivated $[0]_8$, (b) dry pre-activated $[0]_8$, (c) impregnated 20 cSt pre-activated $[0]_8$, (d) impregnated 100 cSt pre-activated $[0]_8$, (e) dry inactivated $[0/45]_4$, (f) dry pre-activated $[0/45]_4$, (g) impregnated 20 cSt pre-activated $[0/45]_4$, and (h) impregnated 100 cSt pre-activated $[0/45]_4$.

to spreading by acting as a lubricant. Moreover, both the three-branch Maxwell and fractional Zener rheological models proved to adequately fit to the Phase II relaxation data obtained from the performed experiments with coefficient of determination values $R2 > 0.92$ for all conditions considered. In contrast, only the latter model proved to sufficiently fit the Phase VI relaxation data (i.e., second relaxation cycle) with coefficient of determination values $R2 > 0.80$ for all conditions. Given that the fractional Zener model is more computationally efficient than the three-branch Maxwell model due to fewer fitting parameters, it is deemed to be better suited for capturing the time-dependent compaction response of the studied fabric. It should be noted that the fitted parameters for both rheological models were not sensitive to small perturbations in the input values during the optimization procedure given that the library used to fit the parameters adds small perturbations as part of the fitting process to avoid premature convergence and convergence to local minima.

The experimental outcomes from this study have enabled an improved understanding of the compaction behavior of infiltrated, binder-stabilized carbon fiber UD-NCFs under different conditions. These outcomes may aid in improving wet compression molding (WCM) processes by guiding the selection of parameters (e.g., binder state and resin viscosity), which can improve the precision in establishing part thickness and, thus, the desired fiber volume fraction. The use of binder-stabilized UD-NCFs in direct WCM processes was proposed in previous work by the authors to enhance resin management, based on an observed increase in bending stiffness of the fabric. Building on this, the present study investigated the effect of binder activation on compaction behavior and found that the time-dependent compaction response is significantly reduced for specimens with pre-activated binder. Thus, future research will investigate the impact of various binder types and binder quantity on the compaction response under various conditions, with the aim of identifying an ideal condition for the pre-activated binder-stabilized UD-NCF for use with a direct WCM process. For the fabric studied, there was no visible interaction between the stabilizing binder and silicon oil used in the compaction experiments. However, when manufacturing a component, it is possible that the binder may be partially dissolved within the resin. Therefore, future efforts will also focus on characterizing the compaction behaviour of the binder-stabilized UD-NCF infiltrated with epoxy resin. Moreover, coupling of the compaction behaviour with the membrane and bending behavior of the fabric will also be explored as these deformation modes are all engaged during fabric forming processes. Previous studies have shown that other dry fabrics exhibit shear-compaction coupling; thus, it would be of interest to understand the extent of this coupled behaviour for an infiltrated fabric with a pre-activated stabilizing binder. Future research will also center on investigating the formability of dry and infiltrated UD-NCF stacks with pre-activated binder. Forming experiments will yield a better understanding of the influence of infiltration state and stabilizing binder activation on the formation of common defects such as wrinkling and local buckling of tows. Finally, the experimental data and parameters derived for the rheological Maxwell and fractional Zener models provide new and important data that can be used as input for material models used in future forming simulations of binder-stabilized UD-NCFs. Recent efforts have shown the importance of capturing the compaction response in macroscopic forming simulations, despite the fact that most forming simulations neglect the fabric compaction mechanism. The data generated in this study could be used to calibrate material models that consider the compaction behaviour of fabrics, which would enhance the fidelity of forming simulations.

CRediT authorship contribution statement

Renan Miranda Portela: Writing – original draft, Validation, Methodology, Investigation, Formal analysis. **Bastian Schäfer:** Writing – review & editing, Methodology, Formal analysis. **Luise Kärger:** Writing – review & editing, Supervision, Resources, Conceptualization. **Alfredo Rocha de Faria:** Writing – review & editing, Validation, Supervision. **John Montesano:** Writing – review & editing, Validation, Supervision, Resources, Project administration, Investigation, Funding acquisition, Conceptualization.

Declaration of competing interest

The authors declare that they have no known competing financial interests or personal relationships that could have appeared to influence the work reported in this paper.

Acknowledgements

This study was funded by the Natural Sciences and Engineering Research Council of Canada (NSERC) through the CREATE grant entitled “Program on Advanced Polymer Composite Materials and Technologies (No. 511011-2018), as well as through a Discovery Grant secured by the corresponding author. Zoltek Corporation is also acknowledged for providing the unidirectional non-crimp fabric that was studied. Finally, the authors thank Cahit Arik, and Kevin Moritz from the Fraunhofer Institute for Chemical Technology, Karlsruhe who provided support in performing the experiments.

Appendix

A.1. Results of statistical assessments

.

Table A1.1
. P-values obtained through the T-Test comparing the maximum compression stress values of inactivated and pre-activated binder-stabilized specimens under different impregnation conditions, for each stacking sequence in both first and second compaction phases (Phases I and VI).

Stacking Sequence	Dry IT x Dry AT	Dry IT x 20 cSt AT	Dry IT x 100 cSt AT	Dry AT x 20 cSt AT	Dry AT x 100 cSt AT	20 cSt AT x 100 cSt AT
$[0]_8$(1st)	0.1858	0.9637	0.3012	0.1911	0.7885	0.2111
$[0/45]_4$(1st)	0.1528	0.9221	0.4093	0.1517	0.0791	0.3727
$[0]_8$(2nd)	0.1710	0.8810	0.3500	0.1616	0.6517	0.2252
$[0/45]_4$(2nd)	0.1203	0.9280	0.3865	0.1214	0.0612	0.3537

Table A1.2
. P-values obtained through T-Test comparing the maximum compression stress values for the first and second compaction phases (Phases I and VI), for each specimen condition.

Configuration	$[0]_8$	$[0/45]_4$
Dry IT	0.1225	0.0617
Dry AT	0.2435	0.1557
20 cSt AT	0.1386	0.0184
100 cSt At	0.1211	0.1489

Table A1.3
. P-values obtained through the T-Test comparing the normalized relaxation stress values of inactivated and pre-activated binder-stabilized specimens under different impregnation conditions, for each stacking sequence in both first and second relaxation (Phases II and VI). Note, green text refers to P-values > 0.05.

Stacking Sequence	Dry IT x Dry AT	Dry IT x 20 cSt AT	Dry IT x 100 cSt AT	Dry AT x 20 cSt AT	Dry AT x 100 cSt AT	20 cSt AT x 100 cSt AT
$[0]_8$(1st)	5.85×10^{-3}	1.40×10^{-2}	4.82×10^{-4}	2.18×10^{-3}	8.30×10^{-7}	3.99×10^{-6}
$[0/45]_4$(1st)	1.06×10^{-6}	5.84×10^{-5}	4.99×10^{-4}	4.53×10^{-3}	7.58×10^{-7}	1.90×10^{-5}
$[0]_8$(2nd)	5.64×10^{-3}	8.63×10^{-1}	5.50×10^{-7}	5.20×10^{-3}	9.86×10^{-7}	1.60×10^{-5}
$[0/45]_4$(2nd)	5.56×10^{-5}	2.88×10^{-3}	2.89×10^{-4}	2.21×10^{-3}	2.25×10^{-5}	1.32×10^{-4}

Table A1.4
. P-values obtained through T-Test comparing the stress relaxation ratio values for the first and second relaxation cycles (Phases II and VI), for each specimen condition.

Configuration	$[0]_8$	$[0/45]_4$
Dry IT	5.29×10^{-3}	4.94×10^{-7}
Dry AT	5.91×10^{-3}	2.89×10^{-5}
20 cSt AT	5.84×10^{-4}	3.78×10^{-4}
100 cSt At	1.03×10^{-7}	1.08×10^{-4}

Table A1.5
. P-values obtained through the T-Test comparing the elastic recovery values of inactivated and pre-activated binder-stabilized specimens under different impregnation conditions, for each stacking sequence, during Phase IV. Note, green text refers to P-values > 0.05.

Stacking Sequence	Dry IT x Dry AT	Dry IT x 20 cSt AT	Dry IT x 100 cSt AT	Dry AT x 20 cSt AT	Dry AT x 100 cSt AT	20 cSt AT x 100 cSt AT
$[0]_8$	6.49×10^{-3}	1.92×10^{-1}	1.30×10^{-3}	1.22×10^{-1}	7.00×10^{-2}	4.44×10^{-3}
$[0/45]_4$	2.50×10^{-2}	8.56×10^{-4}	1.44×10^{-3}	1.04×10^{-1}	2.68×10^{-2}	1.16×10^{-1}

Table A1.6
. P-values obtained through T-Test comparing the maximum compression stress values of the specimens with different stacking sequences in both first and second compaction cycles (Phases I and V), for each condition.

Configuration	$[0]_8$ x $[0/45]_4$ (1st cycle)	$[0]_8$ x $[0/45]_4$ (2nd cycle)
Dry IT	0.2280	0.2549
Dry AT	0.3782	0.4004
20 cSt AT	0.1573	0.1678
100 cSt AT	0.4238	0.4225

Table A1.7
. P-values obtained through T-Test comparing the stress relaxation ratio values of two specimens with different stacking sequences in both first and second compaction cycles (Phases I and V), for each condition. Note, green text refers to P-values > 0.05.

Configuration	$[0]_8$ x $[0/45]_4$ (1st cycle)	$[0]_8$ x $[0/45]_4$ (2nd cycle)
Dry IT	2.34×10^{-1}	3.80×10^{-1}
Dry AT	9.52×10^{-2}	4.03×10^{-2}

(*continued on next page*)

Table A1.7 (*continued*)

Configuration	$[0]_8$ x $[0/45]_4$ (1st cycle)	$[0]_8$ x $[0/45]_4$ (2nd cycle)
20 cSt AT	1.28×10^{-1}	6.09×10^{-2}
100 cSt AT	1.82×10^{-4}	3.18×10^{-3}

Table A1.8
. P-values obtained through the T-Test comparing the elastic recovery rate values for specimens with different stacking sequences, for each condition, during Phase IV.

Configuration	$[0]_8$ x $[0/45]_4$
Dry IT	1.47×10^{-3}
Dry AT	1.05×10^{-1}
20 cSt AT	6.97×10^{-2}
100 cSt AT	6.87×10^{-1}

A.2. Identified model parameters.

.

Table A2.1
. Material parameter values for the fractional Zener model for each condition (Phase II).

Condition	$E_0(\times 10^5)$ [Pa]	$E_1(\times 10^5)$ [Pa]	α	$p(\times 10^5)$ [Pa·s^α]	$f(X)(R^2)$
1	2.172	2.247	0.402	1.671	0.0215 (0.9798)
2	2.565	7.033	0.389	1.605	0.0231 (0.9894)
3	2.286	5.878	0.431	1.545	0.0207 (0.9143)
4	2.084	7.751	0.508	1.722	0.0239 (0.9863)
5	1.973	6.391	0.417	1.495	0.0180 (0.9608)
6	2.368	9.473	0.396	1.486	0.0226 (0.9849)
7	2.023	6.096	0.444	1.461	0.0203 (0.9274)
8	2.321	5.321	0.486	1.898	0.0280 (0.9769)

Table A2.2
. Material parameter values for the Maxwell model for each condition (Phase II).

Cond.	$E_0(\times 10^5)$ [Pa]	$E_1(\times 10^5)$ [Pa]	τ_1 [Pa·s]	$E_2(\times 10^5)$ [Pa]	τ_2 [Pa·s]	$E_3(\times 10^5)$ [Pa]	τ_3 [Pa·s]	$f(X)(R^2)$
1	2.266	2.047	67.72	4.781	4.71	9.071	99.64	0.0296 (0.9744)
2	2.266	4.423	32.72	2.570	52.82	9.354	83.33	0.0174 (0.9363)
3	2.306	0.105	70.23	4.188	3.35	31.259	86.94	0.0244 (0.9655)
4	2.058	2.379	99.81	5.148	3.88	4.600	79.01	0.0247 (0.9429)
5	1.999	0.359	97.32	4.200	2.79	28.913	92.61	0.0320 (0.9875)
6	2.403	0.359	81.89	0.040	70.01	40.976	4.12	0.0284 (0.9729)
7	2.045	0.040	98.61	4.399	3.67	28.437	86.96	0.0387 (0.9444)
8	2.163	0.437	95.38	5.029	3.14	33.360	99.15	0.0316 (0.9749)

Table A2.3
. Material parameter values for the fractional Zener model for each condition (Phase VI).

Conditions	$E_0(\times 10^5)$ [Pa]	$E_1(\times 10^5)$ [Pa]	α	$p(\times 10^5)$ [Pa·s^α]	$f(X)(R^2)$
1	3.721	4.086	0.349	2.194	0.0096 (0.8076)
2	3.989	8.276	0.318	1.816	0.0104 (0.9736)
3	3.538	6.795	0.395	2.008	0.0095 (0.8906)
4	3.715	4.933	0.317	1.566	0.0095 (0.8107)
5	3.500	5.366	0.395	2.161	0.0113 (0.8925)
6	3.724	2.686	0.383	1.900	0.0126 (0.8385)
7	3.115	6.962	0.256	1.243	0.0071 (0.8341)
8	3.932	9.871	0.296	1.741	0.0130 (0.9813)

Table A2.4
. Material parameter values for the Maxwell model for each condition (Phase VI).

Cond.	$E_0(\times 10^5)$ [Pa]	$E_1(\times 10^5)$ [Pa]	τ_1 [Pa·s]	$E_2(\times 10^5)$ [Pa]	τ_2 [Pa·s]	$E_3(\times 10^5)$ [Pa]	τ_3 [Pa·s]	$f(X)(R^2)$
1	3.949	1.607	69.43	2.040	62.26	46.277	6.41	0.0094 (0.9662)
2	4.247	2.477	42.04	1.387	62.33	30.884	4.54	0.0083 (0.8786)
3	3.705	4.995	9.86	0.074	99.18	19.554	68.53	0.0245 (0.7607)
4	3.940	0.564	82.58	3.042	37.81	23.091	1.18	0.0098 (0.5426)
5	3.636	1.325	63.12	3.997	5.58	25.579	76.95	0.0154 (0.8880)
6	3.901	3.183	47.05	0.676	35.05	30.005	1.33	0.0110 (0.7316)
7	3.362	1.155	64.13	1.394	69.47	25.365	5.90	0.0084 (0.9397)
8	4.198	0.009	71.76	3.828	57.19	29.750	1.76	0.0100 (0.8043)

Table A2.5
. Material parameter values for the nonlinear Maxwell model for each condition (Phase I).

Cond.	A	B	a_1	b_1	τ_1	a_2	b_2	τ_2	a_3	b_3	τ_3	R^2
1	394.07	0.22	205.55	57.74	714.79	551.56	73.45	884.58	956.24	87.26	991.15	0.7826
2	234.82	24.56	10.01	78.06	774.41	52.81	4.83	505.24	832.72	76.11	897.55	0.5775
3	456.61	22.51	36.27	2.69	854.27	53.58	12.71	717.58	494.55	7.72	820.84	0.9105
4	474.06	21.33	13.8	1.71	317.88	295.11	35.29	391.69	588.32	25.30	257.40	0.8418
5	255.67	23.09	43.76	63.21	666.38	70.92	0	737.68	938.1	42.52	357.21	0.9803
6	275.71	25.31	4.18	39.63	523.24	146.30	47.57	907.66	233.36	0.67	997.32	0.7341
7	379.37	22.51	238.61	0	508.07	236.88	1.36	408.77	788.2	36.39	495.48	0.8757
8	470.43	22.53	4.20	5.17	358.60	393.38	0.61	230.53	995.24	0	386.00	0.9340

Data availability

Data will be made available on request.

References

[1] C. Poppe, "Process simulation of wet compression moulding for continuous fibre-reinforced polymers," Doctoral Thesis, Karlsruhe Institute of Technology, Karlsruhe, 2021.

[2] Ghazimoradi M, Trejo EA, Carvelli V, Butcher C, Montesano J. Deformation characteristics and formability of a tricot-stitched carbon fiber unidirectional non-crimp fabric. Compos A Appl Sci Manuf 2021;145:106366. https://doi.org/10.1016/J.COMPOSITESA.2021.106366.

[3] Lomov SV, Non-crimp fabric composites. Cambridge, UK: Woodhead Publishing Limited, 2011. doi: 10.1533/9780857092533.

[4] Kärger L, Galkin S, Kunze E, Gude M, Schäfer B. Prediction of forming effects in UD-NCF by macroscopic forming simulation–Capabilities and limitations. ESAFORM 2021–24th International Conference on Material Forming. Belgium: Liège; 2021.

[5] Boisse P, Hamila N, Guzman-Maldonado E, Madeo A, Hivet G, Dell'Isola F. The bias-extension test for the analysis of in-plane shear properties of textile composite reinforcements and prepregs: a review. Int J Mater Form 2017;10:473–92.

[6] Rudd CD, Long AC, Kendall KN, Mangin CGE. Liquid Moulding Technologies. Cambridge, England: Woodhead Publishing Limited, 1997. doi: 10.1533/9781845695446.

[7] Kumar R, Rashvand K, Fraisse A, Sarhadi A, Andersen TL. Experimental testing method to characterise the drapability of UD non-crimp fabrics used in wind turbine blades. IOP Conf Ser: Mater Sci Eng 2023;1293(1):012020. https://doi.org/10.1088/1757-899x/1293/1/012020.

[8] Portela RM, Schafer B, Karger L, de Faria AR, Montesano J. Effect of loading rate, viscosity, and binder activation on the bending response of an infiltrated UD-NCF.

Compos A Appl Sci Manuf 2026;200:109347. https://doi.org/10.1016/J.COMPOSITESA.2025.109347.
[9] Estrada G, Vieux-Pernon C, Advani SG. Experimental characterization of the influence of tackifier material on preform permeability. J Compos Mater 2002;36(19):2297–310. https://doi.org/10.1177/002199830203601954 2.
[10] Brody JC, Gillespie JW. The effects of a thermoplastic polyester preform binder on vinyl ester resin. J Thermoplast Compos Mater 2005;18(3):157–79. https://doi.org/10.1177/0892705705043535.
[11] Yoo HM, Lee JW, Kim JS, Um MK. Influence of non-reactive epoxy binder on the permeability and friction coefficient of twill-woven carbon fabric in the liquid composite molding process. Appl Sci (Switzerland) 2020;10(20):1–13. https://doi.org/10.3390/app10207039.
[12] Bickerton S, Buntain MJ, Somashekar AA. The viscoelastic compression behavior of liquid composite molding preforms. Compos A Appl Sci Manuf 2003;34(5):431–44. https://doi.org/10.1016/S1359-835X(03)00088-5.
[13] Yong AXH, et al. Experimental characterisation of textile compaction response: a benchmark exercise. Compos A Appl Sci Manuf 2021;142:106243. https://doi.org/10.1016/j.compositesa.2020.106243.
[14] Werlen V, Rytka C, Michaud V. A numerical approach to characterize the viscoelastic behaviour of fibre beds and to evaluate the influence of strain deviations on viscoelastic parameter extraction. Compos A Appl Sci Manuf 2021;143. https://doi.org/10.1016/j.compositesa.2021.106315.
[15] Poppe CT, Krauß C, Albrecht F, Kärger L. A 3D process simulation model for wet compression moulding. Compos A Appl Sci Manuf 2021;145:106379. https://doi.org/10.1016/j.compositesa.2021.106379.
[16] Schäfer B, Zheng R, Boisse P, Kärger L. Investigation of the compaction behavior of uni- and bidirectional non-crimp fabrics. In: Materials Research Proceedings. Association of American Publishers; 2023. p. 331–8. https://doi.org/10.21741/9781644902479-36.
[17] Li L, Zhao Y, Yang J, Zhang J, Duan Y. An experimental investigation of compaction behavior of carbon non-crimp fabrics for liquid composite molding. J Mater Sci 2015;50(7):2960–72. https://doi.org/10.1007/s10853-015-8860-0.
[18] Droste D, et al. Investigation of the compaction behaviour of a quasi-unidirectional non-crimp fabric during the vacuum infusion process. J Compos Mater 2022;56(16):2509–24. https://doi.org/10.1177/00219983221092011.
[19] Wei K, Liang D, Mei M, Yang X, Chen L. A viscoelastic model of compression and relaxation behaviors in preforming process for carbon fiber fabrics with binder. Compos B Eng 2019;158:1–9. https://doi.org/10.1016/j.compositesb.2018.09.038.
[20] Wei K, Liang D, Mei M, Wang D, Yang X, Qu Z. Preforming behaviors of carbon fiber fabrics with different contents of binder and under various process parameters. Compos B Eng 2019;166:221–32. https://doi.org/10.1016/j.compositesb.2018.11.143.
[21] Robitaille F, Gauvin R. Compaction of textile reinforcements for composites manufacturing. I: review of experimental results. Polymer Compos 1998;19(2):198–216.
[22] Gutowski TG, Cai Z, Bauer S, Boucher D, Kingery J, Wineman S. Consolidation experiments for laminate composites. J Compos Mater 1987;21(7):650.
[23] Mitsch J, Schäfer B, Kärger L. Rate-dependent 3D forming simulation of thermoplastic composite materials using visco-hyperelastic material modeling and 3D hexahedral solid-shell elements. Compos A Appl Sci Manuf 2026;200:109306. https://doi.org/10.1016/J.COMPOSITESA.2025.109306.
[24] Ding K, Xiao Y. Adaptability of burgers rheological model and its improved model to the creep properties of glue laminated bamboo. Mechanika 2024;30(3):214–20. https://doi.org/10.5755/j02.mech.35600.
[25] Moutee M, Student G, Fafard M, Fortin Y, Laghdir A. Modeling the creep behavior of wood cantilever loaded at free end during drying. Wood Fiber Sci 2005;37(3):521–34.
[26] Jelić S, Zorica D. Fractionalization of anti-Zener and Zener models via rheological analogy. Acta Mech 2023;234(2):313–54. https://doi.org/10.1007/s00707-022-03363-8.
[27] Echaabi J, Nziengui MB, Hattabi M. Compressibility and relaxation models for fibrous reinforcements in Liquid Composites Moulding. Int J Mater Form 2008;1(S1):851–4. https://doi.org/10.1007/s12289-008-0269-8.
[28] Danzi M, Schneeberger C, Ermanni P. A model for the time-dependent compaction response of woven fiber textiles. Compos A Appl Sci Manuf 2018;105:180–8. https://doi.org/10.1016/j.compositesa.2017.11.002.
[29] Haveroth TCDC, "On The Use Of Fractional Derivatives For Modeling Nonlinear Viscoelasticity," Master Thesis, Universidade do Estado de Santa Catarina, Joinville, 2015.
[30] da Costa-Haveroth TC, et al. Aspects on viscoelasticity modeling of HDPE using fractional derivatives: Interpolation procedures and efficient numerical scheme. Mech Adv Mater Struct 2022;29(25):4343–58. https://doi.org/10.1080/15376494.2021.1928345.
[31] Padovan J. Computational algorithms for FE formulations involving fractional operators. Comput Mech 1987;2(4):271–87. https://doi.org/10.1007/BF00296422.
[32] Ferrante M. Viscoelastic models for the simulation of transients in polymeric pipes. J Hydraul Res 2017;55(5):599–612. https://doi.org/10.1080/00221686.2017.1354935.
[33] Kühl A, "Uma Formulação Viscoelastoplástica Não Linear Aplicada ao Polietileno de Alta Densidade (PEAD)," Master Thesis, Universidade do Estado de Santa Catarina, 2014.
[34] Bai Q, Analysis of Particle Swarm Optimization Algorithm, Computer and Information Science, 2010;3(1), doi: 10.5539/cis.v3n1p180.
[35] Bublitz D, Colin D, Drechsler K. Implementation of a viscoelastic material model to predict the compaction response of dry carbon fiber preforms. Compos A Appl Sci Manuf 2022;153:106718. https://doi.org/10.1016/J.COMPOSITESA.2021.106718.
[36] Careglio CA, Canales C, Papeleux L, Ponthot J-P, Mirasso AE. An implementation of the generalized maxwell viscoelastic constitutive model. Mecánica Computacional 2014;XXXIII(1215):1179–92.
[37] Roylance D, "Engineering Viscoelasticity," 2001, Department of Materials Science and Engineering – Massachusetts Institute of Technology, Cambridge, MA.
[38] Schmidt A, Gaul L. On the numerical evaluation of fractional derivatives in multi-degree-of-freedom systems. Signal Process 2006;86(10):2592–601. https://doi.org/10.1016/j.sigpro.2006.02.006.
[39] Liu H, Polak MA, Penlidis A. A practical approach to modeling time-dependent nonlinear creep behavior of polyethylene for structural applications. Polym Eng Sci 2008;48(1):159–67. https://doi.org/10.1002/pen.20942.
[40] Blank J, Deb K. Pymoo: multi-objective optimization in python. IEEE Access 2020;8:89497–509. https://doi.org/10.1109/ACCESS.2020.2990567.
[41] Song C, Kawai R. Monte Carlo and variance reduction methods for structural reliability analysis: a comprehensive review. Probab Eng Mech 2023;73:103479. https://doi.org/10.1016/j.probengmech.2023.103479.
[42] Grieser T, Mitschang P. Investigation of the compaction behavior of carbon fiber NCF for continuous preforming processes. Polym Compos 2017;38(11):2609–25. https://doi.org/10.1002/pc.23854.
[43] Lomov SV, Verpoest I, Peeters T, Roose D, Zako M. Nesting in textile laminates: geometrical modelling of the laminate. Compos Sci Technol 2003;63(7):993–1007. https://doi.org/10.1016/S0266-3538(02)00318-4.
[44] Portela RM, Schäfer B, Kärger L, Rocha De Faria A, Montesano J. Influence of Viscosity, Binder Activation, and Loading Rate on the Membrane Response of an Infiltrated UD-NCF,In: ESAFORM 2024–27th International Conference on Material Forming Toulouse, 2024.
[45] Kaliske M, Rothert H. Formulation and implementation of three-dimensional viscoelasticity at small and finite strains. Comput Mech 1997;19(3):228–39. https://doi.org/10.1007/s004660050171.